



1 **Atmospheric energy budget response to idealized aerosol perturbation in**
2 **tropical cloud systems**

3 **Guy Dagan¹, Philip Stier¹, Matthew Christensen¹, Guido Cioni^{2,3}, Daniel Klocke^{3,4} and Axel**
4 **Seifert⁴**

5 ¹ Atmospheric, Oceanic and Planetary Physics, Department of Physics, University of Oxford, UK

6 ² Max Planck Institute for Meteorology, Hamburg, Germany

7 ³ Hans Ertel Center for Weather Research, Offenbach am Main, Germany

8 ⁴ Deutscher Wetterdienst, Offenbach am Main, Germany

9 E-mail: guy.dagan@physics.ox.ac.uk

10

11 **Abstract**

12 The atmospheric energy budget is analysed in numerical simulations of tropical cloud systems.
13 This is done in order to better understand the physical processes behind aerosol effects on the
14 atmospheric energy budget. The simulations include both shallow convective clouds and deep
15 convective tropical clouds over the Atlantic Ocean. Two different sets of simulations, at different
16 dates (10-12/8/2016 and 16-18/8/2016), are being simulated with different dominant cloud
17 modes (shallow or deep). For each case, the cloud droplet number concentrations (CDNC) is
18 varied as a proxy for changes in aerosol concentrations. It is shown that the total column
19 atmospheric radiative cooling is substantially reduced with CDNC in the deep-cloud dominated
20 case (by ~ 10.0 W/m²), while a much smaller reduction (~ 1.6 W/m²) is shown in the shallow-
21 cloud dominated case. This trend is caused by an increase in the ice and water vapor content at
22 the upper troposphere that leads to a reduced outgoing longwave radiation. A decrease in sensible
23 heat flux (driven by increase in the near surface air temperature) reduces the warming by ~ 1.4
24 W/m² in both cases. It is also shown that the cloud fraction response behaves in opposite ways
25 to an increase in CDNC, showing an increase in the deep-cloud dominated case and a decrease
26 in the shallow-cloud dominated case. This demonstrates that under different environmental
27 conditions the response to aerosol perturbation could be different.

28

29



30 **Introduction**

31 The negative anthropogenic radiative forcing due to aerosols is acting to cool the climate and to
32 compensate some of the warming due to increase in greenhouse gases (Boucher et al., 2013).
33 However, quantification of this effect is highly uncertain with a revised uncertainty range of
34 -1.60 to -0.65 W/m^2 (Bellouin et al., 2019). The total anthropogenic aerosol radiative forcing is
35 composed of contribution from direct interaction of aerosols with radiation (scattering and
36 absorption) and from indirect interaction with radiation due to changes in cloud properties.

37 Beside its effect on the radiation budget, aerosols may affect the precipitation distribution and
38 total amount (Levin and Cotton, 2009; Albrecht, 1989; Tao et al., 2012). A useful perspective to
39 improve our understanding of aerosol effect on precipitation, which became common in the last
40 few years, arises from constraints on the energy budget (O’Gorman et al., 2012; Muller and
41 O’Gorman, 2011; Hodnebrog et al., 2016; Samset et al., 2016; Myhre et al., 2017; Liu et al.,
42 2018; Richardson et al., 2018; Dagan et al., 2019a). On long time scales, any precipitation
43 perturbations by aerosol effects will have to be balanced by changes in radiation fluxes, sensible
44 heat flux or by divergence of dry static energy. The energy budget constraint perspective was
45 found useful to explain both global (e.g. (Richardson et al., 2018)) and regional (Liu et al., 2018;
46 Dagan et al., 2019a) precipitation response to aerosol perturbations in global scale simulations.
47 In this study, we investigate the energy budget response to aerosol perturbation on a regional
48 scale using high resolution cloud resolving simulations. This enables an improved understanding
49 of the microphysical processes controlling atmospheric energy budget perturbations. The strong
50 connection between the atmospheric energy budget and convection has long been appreciated
51 (e.g. (Arakawa and Schubert, 1974; Manabe and Strickler, 1964)) as well as the connection to
52 the general circulation of the atmosphere (Emanuel et al., 1994).

53 The total column atmospheric energy budget can be described as follows:

$$54 \quad LP + Q_R + Q_{SH} = \text{div}(s) + ds/dt \quad (1)$$

55 Equation 1 presents a balance between the latent heating rate (LP - latent heat of condensation
56 [L] times the surface precipitation rate [P]), the surface sensible heat flux (Q_{SH}), the atmospheric
57 radiative heating (Q_R), the divergence of dry static energy ($\text{div}(s)$, which will become negligible
58 on sufficiently large spatial scales), and dry static energy storage term (ds/dt , which will become
59 negligible on long [inter-annual] temporal scales). Throughout the rest of this paper we will refer
60 to the right-hand side of Equation 1 ($\text{div}(s) + ds/dt$) as the residual (R) of the left-hand side.



61 Q_R is defined as:

$$62 \quad Q_R = (F_{SW}^{TOA} - F_{SW}^{SFC}) + (F_{LW}^{TOA} - F_{LW}^{SFC}) \quad (2)$$

63 and represents the rate of net atmospheric diabatic warming due to radiative shortwave (SW) and
64 longwave (LW) fluxes. It is expressed by the sum of the surface (SFC) and top of the atmosphere
65 (TOA) fluxes, when all fluxes are positive downwards. As in the case of TOA radiative forcing,
66 aerosols could modify the atmospheric energy budget by both direct interaction with radiation
67 and by microphysical effects on clouds. The latter is the focus of this study.

68 The microphysical effects are driven by the fact that aerosols serve as cloud condensation nuclei
69 (CCN) and ice nuclei (IN). Larger aerosol concentrations, e.g. by anthropogenic emissions, could
70 lead to larger cloud droplet and ice particle concentrations (Andreae et al., 2004; Twomey, 1977;
71 Hoose and Möhler, 2012). Changes in hydrometer concentration and size distribution were
72 shown to affect clouds' microphysical processes rates (such as condensation, evaporation,
73 freezing and collision-coalescence), which in turn could affect the dynamics of the clouds (Khain
74 et al., 2005; Koren et al., 2005; Heikenfeld et al., 2019; Chen et al., 2017; Altaratz et al., 2014;
75 Seifert and Beheng, 2006a), the rain production (Levin and Cotton, 2009; Albrecht, 1989; Tao
76 et al., 2012) and the clouds' radiative effect (Koren et al., 2010; Storelvmo et al., 2011; Twomey,
77 1977; Albrecht, 1989). The aerosol effect, and in particular its effects on the radiation budget
78 and the atmospheric energy budget, is cloud regime dependent (Altaratz et al., 2014; Lee et al.,
79 2009; Mülmenstädt and Feingold, 2018; van den Heever et al., 2011; Rosenfeld et al., 2013;
80 Glassmeier and Lohmann, 2016; Gryspeerd and Stier, 2012; Christensen et al., 2016), time
81 dependent (Dagan et al., 2017; Gryspeerd et al., 2015; Seifert et al., 2015; Lee et al., 2012;
82 Dagan et al., 2018c), aerosol type and size distribution dependent (Jiang et al., 2018; Lohmann
83 and Hoose, 2009) and (even for a given cloud regime) meteorological conditions dependent
84 (Dagan et al., 2015a; Fan et al., 2009; Fan et al., 2007; Kalina et al., 2014; Khain et al., 2008)
85 and was shown to be non-monotonic (Dagan et al., 2015b; Joon et al., 2018; Gryspeerd et al.,
86 2019; Liu et al., 2019). Hence the quantification of the global mean radiative effect is extremely
87 challenging (e.g. (Stevens and Feingold, 2009; Bellouin et al., 2019)).

88 Previous studies demonstrated that the mean aerosol effect on deep convective clouds can
89 increase the upward motion of water, and hence also increase the cloud anvil mass and extent
90 (Fan et al., 2010; Chen et al., 2017; Fan et al., 2013; Grabowski and Morrison, 2016). The
91 increase in mass flux to upper levels was explained by the convective invigoration hypothesis
92 (Fan et al., 2013; Koren et al., 2005; Rosenfeld et al., 2008; Seifert and Beheng, 2006a; Yuan et



93 al., 2011a; Williams et al., 2002), which was proposed to lead to stronger latent heat release
94 under higher aerosol concentrations and hence stronger vertical velocities. In addition to the
95 stronger vertical velocities, under polluted conditions the smaller hydrometers are being
96 transported higher in the atmosphere (for a given vertical velocity (Chen et al., 2017; Koren et
97 al., 2015; Dagan et al., 2018a)) and their lifetime at the upper troposphere is longer (Fan et al.,
98 2013; Grabowski and Morrison, 2016). The invigoration mechanism can also lead to an increase
99 in precipitation (Khain, 2009; Altaratz et al., 2014). Both the increase in precipitation and the
100 increase in anvil coverage would act to warm the atmospheric column: the increased precipitation
101 by latent heat release, and the increased anvil mass and extent by longwave radiative warming
102 (Koren et al., 2010; Storelvmo et al., 2011). However, it should be pointed out that the
103 uncertainty underlying these proposed effects remain significant (White et al., 2017; Varble,
104 2018). In addition, aerosol effects on precipitation from deep convective cloud was shown to be
105 non-monotonic and depend on the aerosol range (Liu et al., 2019).

106 In the case of shallow clouds, aerosol effect on precipitation was also shown to be non-monotonic
107 (Dagan et al., 2015a; Dagan et al., 2017). However, unlike in the deep clouds case, the mean
108 effect on precipitation, under typical modern-day conditions, is thought to be negative (Albrecht,
109 1989; Rosenfeld, 2000; Jiang et al., 2006; Xue and Feingold, 2006; Dagan and Chemke, 2016).
110 The aerosol effect on shallow cloud cover and mean water mass (measure by liquid water path -
111 LWP) might also depend on the meteorological conditions and aerosol range (Dagan et al.,
112 2015b; Dagan et al., 2017; Gryspeerdt et al., 2019; Dey et al., 2011; Savane et al., 2015) and is
113 the outcome of competition between different opposing response of: rain suppression (that could
114 lead to increase in cloud lifetime and coverage (Albrecht, 1989)), warm clouds invigoration (that
115 could also lead to increase in cloud coverage and LWP (Koren et al., 2014; Kaufman et al., 2005;
116 Yuan et al., 2011b)) and increase in entrainment and evaporation (that could lead to decrease in
117 cloud coverage (Small et al., 2009; Jiang et al., 2006; Costantino and Bréon, 2013; Seigel, 2014)).
118 Another addition to this complex response is the fact that the aerosol effect on warm convective
119 clouds was shown to be time dependent and affected by the clouds' feedbacks on the
120 thermodynamic conditions (Seifert et al., 2015; Dagan et al., 2016; Dagan et al., 2017; Lee et al.,
121 2012; Stevens and Feingold, 2009; Dagan et al., 2018b). Previous simulations that contained
122 several tropical cloud modes demonstrate that increase in aerosol concentrations can lead to
123 suppression of the shallow mode and invigoration of the deep mode (van den Heever et al., 2011).
124 Hence the domain mean effect, even if it is demonstrated to be small, may be the result of
125 opposing relatively large contributions from the different cloud modes (van den Heever et al.,



126 2011). The small domain mean effect may suggest that on large enough scales the energy (Muller
127 and O’Gorman, 2011; Myhre et al., 2017) or water budget (Dagan et al., 2019b) constrain
128 precipitation changes.

129 Previous studies, using global simulations (O’Gorman et al., 2012; Muller and O’Gorman, 2011;
130 Hodnebrog et al., 2016; Samset et al., 2016; Myhre et al., 2017; Liu et al., 2018; Richardson et
131 al., 2018; Dagan et al., 2019a), demonstrated the usefulness of the atmospheric energy budget
132 perspective in constraining aerosol effect on precipitation. However, the physical processes
133 behind aerosol-cloud microphysical effects on the energy budget are still far from being fully
134 understood. In this study we use cloud resolving simulations to increase our understanding of the
135 effect of microphysical aerosol-cloud interactions on the atmospheric energy budget.

136 **Methodology**

137 The icosahedral nonhydrostatic (ICON) atmospheric model (Zängl et al., 2015) is used in a
138 limited area configuration. ICON’s non-hydrostatic dynamical core was evaluated with several
139 idealized cases (Zängl et al., 2015). The simulations are conducted such that they are aligned
140 with the NARVAL 2 (Next-generation Aircraft Remote-Sensing for Validation Studies (Klepp
141 et al., 2014; Stevens et al., 2019; Stevens et al., 2016)) campaign, which took place during August
142 2016 in the western part of the northern tropical Atlantic. We use existing NARVAL 2
143 convection-permitting simulations (Klocke et al., 2017) as initial and boundary conditions for
144 our simulations.

145 The domain covers $\sim 22^\circ$ in the zonal direction ($25^\circ - 47^\circ$ W) and $\sim 11^\circ$ in the meridional direction
146 ($6^\circ - 17^\circ$ N) and therefore a large fraction of the northern tropical Atlantic (Fig. 1). During August
147 2016, the intertropical convergence zone (ITCZ) was located in the southern part of the domain
148 while the northern part mostly contains trade cumulus clouds. Hence, this case study provides
149 an opportunity to study heterogenous clouds systems. Daily variations in the deep/shallow cloud
150 modes in our domain were observed, but it always included both cloud modes, albeit in different
151 relative fraction. Two different dates are chosen, one representing a shallow-cloud dominated
152 mode (10-12/8/2016 – see Fig. 2, and Figs S1 and S3, supporting information- SI), and one that
153 represents a deep-cloud dominated mode (16-18/8/16 – see Fig. 3 and Figs. S2 and S3, SI). In
154 the shallow-cloud dominated case, most of the domain is covered by trade cumulus clouds that
155 are being advected with the trade winds from north-east to south-west. In the southern part of the
156 domain, throughout most of the simulation, there is a zonal band of deep convective clouds (Fig.



157 2) that contribute on average ~25% out of the total cloud cover (Fig. S3, SI). The deep-cloud
158 dominated case represents the early stages of the development of the tropical storm Fiona (Fig.
159 3). Fiona formed in the eastern tropical Atlantic and moved toward the west-north-west. It started
160 as a tropical depression at 16/8/2016 18:00 UTC while its centre was located at 12.0° N 32.2° W.
161 It kept moving towards the north-west and reach a level of a tropical storm at 17/8/2016 12UTC,
162 while its centre was located at 13.7° N 36.0° W
163 (https://www.nhc.noaa.gov/data/tcr/AL062016_Fiona.pdf). The general propagation speed and
164 direction, strength (measure by maximal surface wind speed) and location of the storm are
165 predicted well by the model. However, the model produces more anvil clouds than what was
166 observed from the satellite (Fig. 3). These two different cases, representing different atmospheric
167 energy budget initial state (see also Figs. 4 and 12 below), enable the investigation of the aerosol
168 effect on the energy budget under different initial conditions.

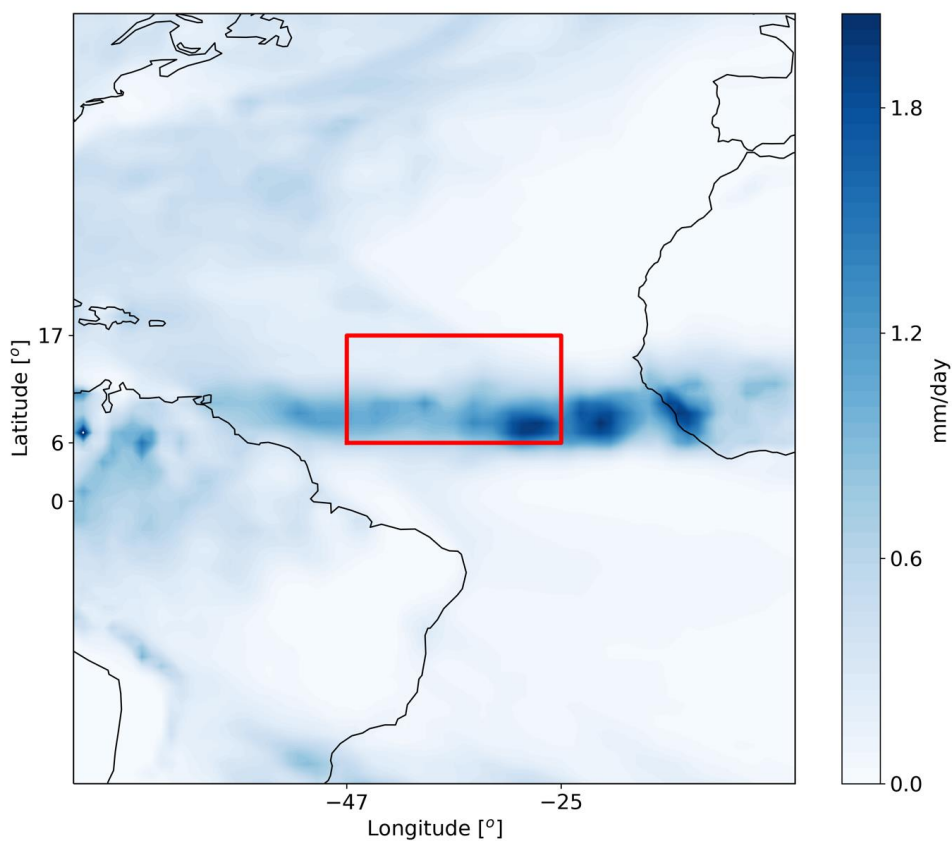
169 We use a two-moment bulk microphysical scheme (Seifert and Beheng, 2006b). For each case,
170 four different simulations with different prescribed cloud droplet number concentrations
171 (CDNC) of 20, 100, 200, and 500 cm⁻³ are conducted. The different CDNC scenarios serve as
172 a proxy for different aerosol concentration conditions (as the first order effect of increased
173 aerosol concentration is to increase the CDNC (Andreae, 2009)) and avoid the uncertainties
174 involved in the representation of the aerosols in numerical models (Ghan et al., 2011; Simpson
175 et al., 2014; Rothenberg et al., 2018). However, it limits potential feedbacks between clouds
176 and aerosols, such as the removal of aerosol levels by precipitation scavenging and potential
177 aerosol effects thereon. In addition, the fix CDNC framework does not capture the differences
178 in aerosol activation fraction between shallow and deep clouds, due to differences in vertical
179 velocity.

180 For calculation of the difference between high CDNC (polluted) conditions and low CDNC
181 (clean) conditions, the simulations with CDNC of 200 and 20 cm⁻³ are chosen as they represent
182 the range typically observed over the ocean (see for example the CDNC range presented in
183 recent observational-based studies (Rosenfeld et al., 2019; Gryspeerdt et al., 2019)). Each
184 simulation is conducted for 48 hours starting from 12 UTC. The horizontal resolution is set to
185 1200 m and 75 vertical levels are used. The temporal resolution is 12 sec and the output interval
186 is 30 min. Interactive radiation is calculated every 12 min using the RRTM-G scheme (Clough
187 et al., 2005; Iacono et al., 2008; Mlawer et al., 1997). We have added a coupling between the
188 microphysics and the radiation to include the Twomey effect (Twomey, 1977). This was done



189 by including the information of the cloud liquid droplet effective radius, calculated in the
190 microphysical scheme, in the radiation calculations. No Twomey effect due to changes in the
191 ice particles size distribution was considered due to the large uncertainty involved in the ice
192 microphysics and morphology. Additional details, such as the surface and atmospheric physics
193 parameterizations, are described in Klocke et al., (2017) and include an interactive surface flux
194 scheme and a fixed sea surface temperature.

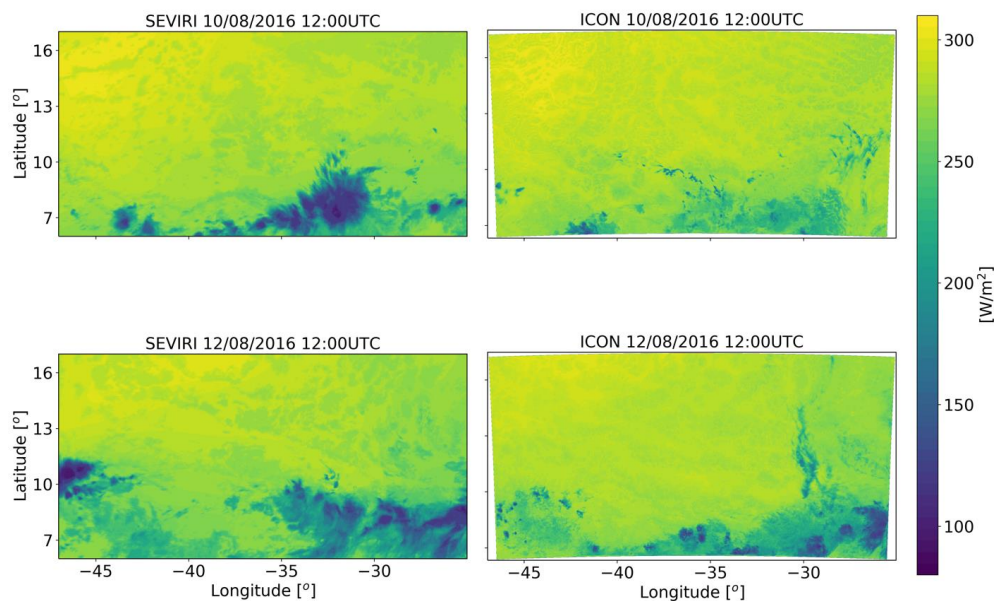
195 For comparing the outgoing longwave flux from the simulations and observations we use
196 imager data from the SEVIRI instrument onboard the Meteosat Second Generation (MSG)
197 geostationary satellite (Aminou, 2002). The outgoing longwave flux is calculated using the
198 Optimal Retrieval for Aerosol and Cloud (ORAC) algorithm (Sus et al. 2017; McGarragh, et
199 al. 2017). Cloud optical (thickness, effective radius, water path) and thermal (cloud top
200 temperature and pressure) properties are retrieved from ORAC using an optimal estimation-
201 based approach. These retrievals and reanalysis profiles of temperature, humidity and ozone
202 are then ingested into BUGSrad, a two-stream correlated-k broadband flux algorithm (Stephens
203 et al., 2001) that outputs the fluxes at the top and bottom of the atmosphere and shown to have
204 excellent agreement when applied to both active (CloudSat) and passive (Advanced Along
205 Track Scanning Radiometer) satellite sensors compared to Clouds and the Earth's Radiant
206 Energy System (Henderson et al. 2013; Stengel et al. 2019). In addition, off-line sensitivity
207 radiative transfer tests using vertical profiles from our model were conducted with BUGSrad
208 to identify the source of the differences in fluxes between clean and polluted conditions.



209

210 **Figure 1. Domain of the ICON simulations (red rectangle) for the NARVAL 2 case study overlaid on the**
211 **August 2016 ECMWF era-interim reanalysis (Dee et al., 2011) mean precipitation rate.**

212

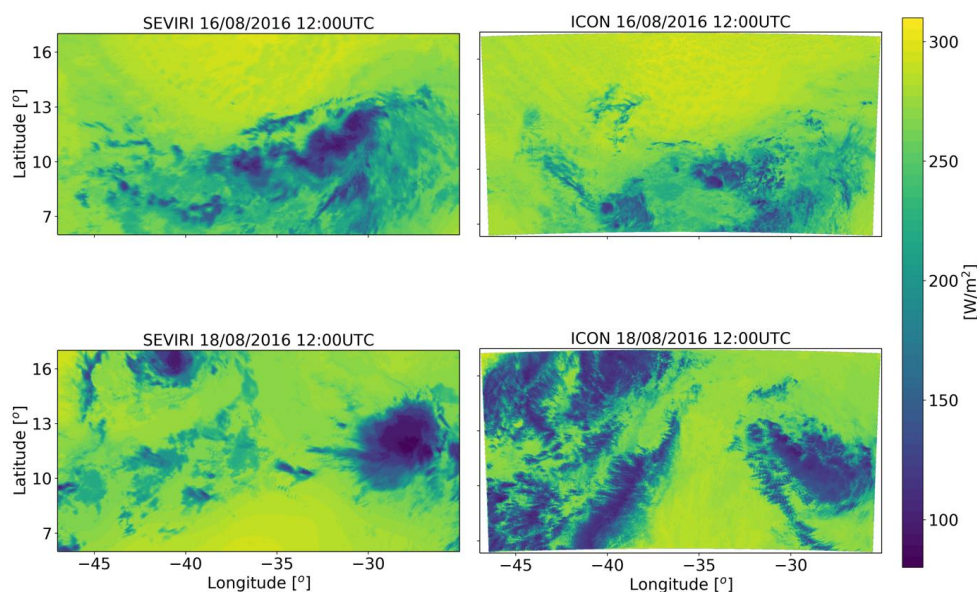


213

214 **Figure 2. Outgoing longwave flux at the top of atmosphere at the initial stage (upper row) and the last stage**
215 **(lower row – each average over 30 minutes) of the simulation of the shallow-cloud dominated case (10-**
216 **12/08/2016) from geo-stationary satellite (SEVIRI-MSG – right column) and the ICON model simulation with**
217 **CDNC of 20 cm⁻³ (left column).**

218

219



220

221 **Figure 3. similar to Figure 2 but for the deep-cloud dominated case.**

222 **Results**

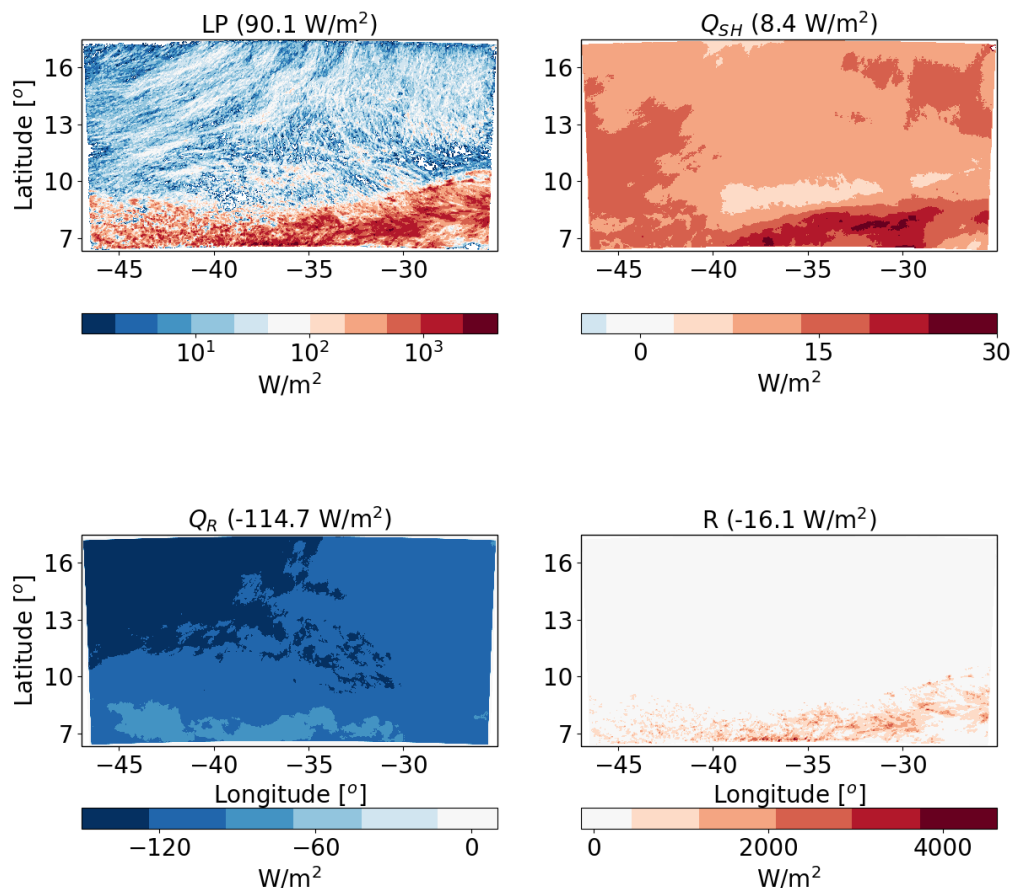
223 **Shallow-cloud dominated case -10-12/08/2016**

224 We start with energy budget analysis of the shallow-cloud dominated case base simulations
225 ($CDNC = 20 \text{ cm}^{-3}$). Figure 4 presents the time mean (over the two days simulation) of the
226 different terms of the energy budget (Equation 1). As expected, LP dominates the warming of
227 the atmosphere while Q_R dominate the cooling. The sensible heat flux (Q_{SH}) is positive (act to
228 warm the atmosphere) but it is an order of magnitude smaller than the LP and Q_R magnitudes. In
229 this shallow-cloud dominated case the radiative cooling of the atmosphere is significantly larger
230 than the warming due to precipitation (mean of -114.7 W/m^2 compare with 90.1 W/m^2), hence
231 the residual (R) is negative. Negative R means that there must be some convergence of dry static
232 energy into the domain and/or decrease in the storage term.

233 We note that there is a significant difference in the spatial distribution of LP and Q_R (Jakob et
234 al., 2019). While the Q_R is more uniformly distributed, the LP is mostly concentrated at the south
235 part of the domain (where the deep convective clouds are formed) and it has a dotted structure.
236 Locally, at the core of a deep convective clouds, the LP contribution can reach a few 1000 W/m^2
237 (1 mm/hr of precipitation is equivalent to 628 W/m^2), however, the vast majority of the domain
238 contributes very little in terms of LP . Q_R also presents some spatial structure in which there is a



239 weak atmospheric cooling at the south part of the domain (the region of the deep convective
240 clouds) and a strong cooling at the reset of the domain.



241

242 **Figure 4.** Spatial distribution of the time mean of the different terms of the energy budget for the ICON
243 simulation of the shallow-cloud dominated case (10-12/08/2016) with $CDNC = 20 \text{ cm}^{-3}$. The terms that appear
244 here are: LP - latent heat by precipitation, Q_{SH} - sensible heat flux, Q_R - atmospheric radiative warming, and
245 R - the residual. The domain and time-mean value of each term appears in parenthesis.

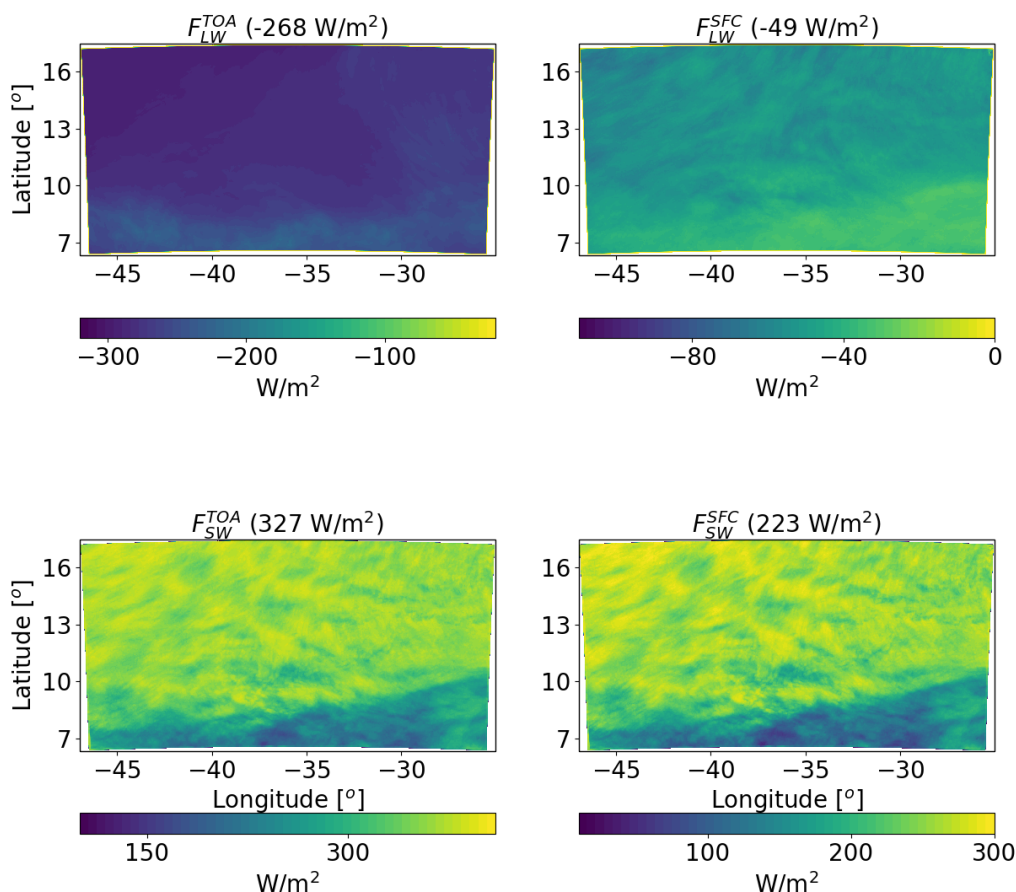
246

247 For understanding the spatial structure of Q_R , next we examine the spatial distribution of the LW
248 and SW radiative fluxes at the TOA and surface (Fig. 5). We note that the smaller radiative
249 cooling in the region of deep clouds in the south of the domain is mostly contributed by a
250 decrease in F_{LW}^{TOA} . The SW fluxes also demonstrate a strong south-north gradient, as the deep



251 convective clouds in the south are more reflective than the shallow trade cumulus (with the lower
252 mean cloud fraction) in the rest of the domain.

253



254

255 **Figure 5. Spatial distribution of ICON simulated time-mean longwave (LW) and shortwave (SW) radiation**
256 **fluxes at the top of atmosphere (TOA) and surface (SFC) for a simulation of the shallow-cloud dominated**
257 **case (10-12/08/2016) with CDNC = 20 cm⁻³. The domain and time mean value of each term appears in**
258 **parenthesis.**

259

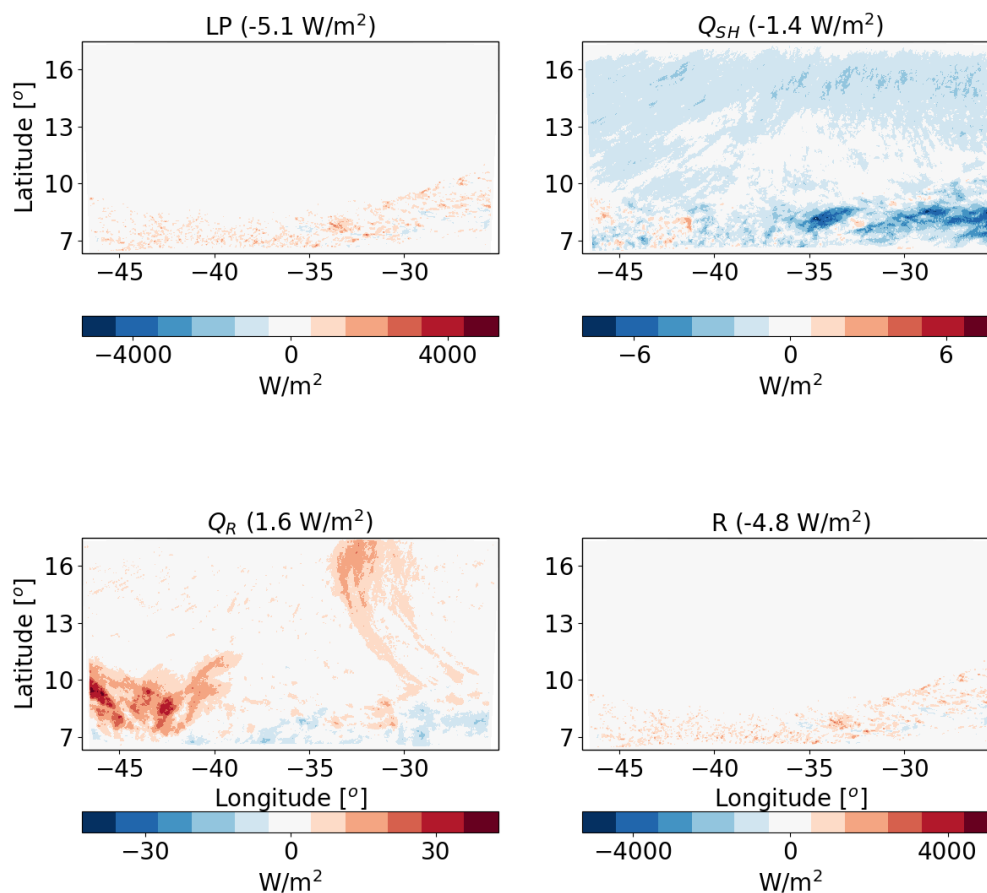
260 **Response to aerosol perturbation – shallow-cloud dominated case**

261 Next, we analyse the response of the atmospheric energy budget of this case to perturbations in
262 CDNC. Figure 6 presents the differences in the different terms of the energy budget between a



263 polluted simulation ($CDNC = 200 \text{ cm}^{-3}$) and a clean simulation ($CDNC = 20 \text{ cm}^{-3}$). It
264 demonstrates that the LP differences between the different $CDNC$ scenarios contribute 5.1 W/m^2
265 less to warm the atmosphere in the polluted vs. the clean simulation. We note that this apparently
266 large effect is caused by a small, non-statistically significant, precipitation difference ($\sim 0.4 \text{ mm}$
267 over the two days of simulation - see Fig. 8 below). The strong sensitivity of the atmospheric
268 energy budget to small precipitation changes (recalling that 1 mm/hr is equivalent to 628 W/m^2)
269 exemplifies the caution one needs to take when looking on precipitation response in terms of
270 energy budget perspective. The Q_R differences lead to relative warming of the atmosphere of the
271 polluted case compared to the clean case by 1.6 W/m^2 . We note that most of the Q_R differences
272 are located in the south-west part of the domain. The Q_{SH} changes counteracts 1.4 W/m^2 of the
273 atmospheric warming by Q_R and so the end result is a deficit of 4.8 W/m^2 in the atmospheric
274 energy budget in the polluted simulation compared to the clean simulation. The decrease in the
275 Q_{SH} is driven by an increase in the near surface air temperature (see Fig. 8).

276



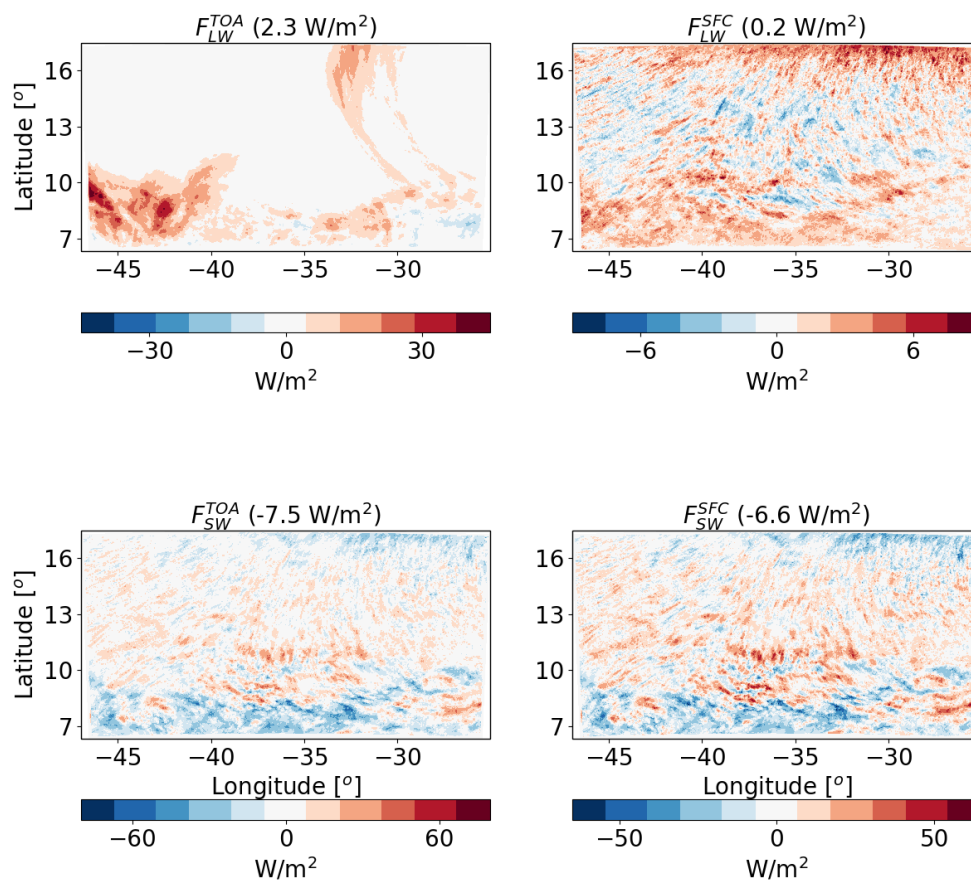
277

278 **Figure 6.** The differences between polluted ($\text{CDNC} = 200 \text{ cm}^{-3}$) and clean ($\text{CDNC} = 20 \text{ cm}^{-3}$) ICON simulations
279 of the time-mean terms of the energy budget for the shallow-cloud dominated case (10-12/08/2016). The terms
280 that appears here are: *LP* - latent heat by precipitation, *Q_{SH}* - sensible heat flux, *Q_R* - atmospheric radiative
281 warming, and **R** – the residual. The domain and time mean value of each term appears in parenthesis.

282 To understand the response of *Q_R* to the CDNC perturbation, we next examine the response of
283 the different radiative fluxes. Figure 7 demonstrates that most of the relative atmospheric
284 radiative heating in the polluted case compared to the clean case is contributed by changes in the
285 F_{LW}^{TOA} fluxes. The changes in F_{LW}^{SFC} are an order of magnitude smaller. The SW fluxes change both
286 at the TOA and SFC are larger than the F_{LW}^{TOA} changes, however, in terms of the atmospheric energy
287 budget, they almost cancel each other out and the net SW atmospheric effect is only -0.9 W/m^2 .
288 Most of the reduction in SW fluxes (both at TOA and the surface) comes from the deep
289 convective regions in the south of the domain while the shallow cloud regions experience some
290 increase in SW fluxes. This can be attributed to the increase in deep convective cloud fraction



291 and a decrease in the shallow cloud fraction with the increase in CDNC (see Fig. 9 below). The
292 TOA net radiative effect for the entire system (as opposed to the atmospheric energy budget that
293 take into consideration the surface radiative fluxes changes) is about -5.2 W/m^2 .



294
295 **Figure 7.** The differences between polluted ($\text{CDNC} = 200 \text{ cm}^{-3}$) and clean ($\text{CDNC} = 20 \text{ cm}^{-3}$) ICON simulations
296 of the time mean radiative longwave (LW) and shortwave (SW) fluxes at the top of atmosphere (TOA) and
297 and surface (SFC) for the shallow-cloud dominated case (10-12/08/2016). The domain and time mean value of
298 each term appears in parenthesis.

299

300 The differences in the energy (Fig. 6) and radiation (Fig. 7) budgets between the clean and
301 polluted cases shown above, could be explained by the differences in the cloud mean properties.
302 Figure 8 presents the time evolution of some of the domain mean properties while Fig. 9 presents
303 time and horizontal mean vertical profiles. To examine the robustness of the trends we add here
304 two more CDNC cases of 100 and 500 cm^{-3} (on top of the two that were examine above – 20 and



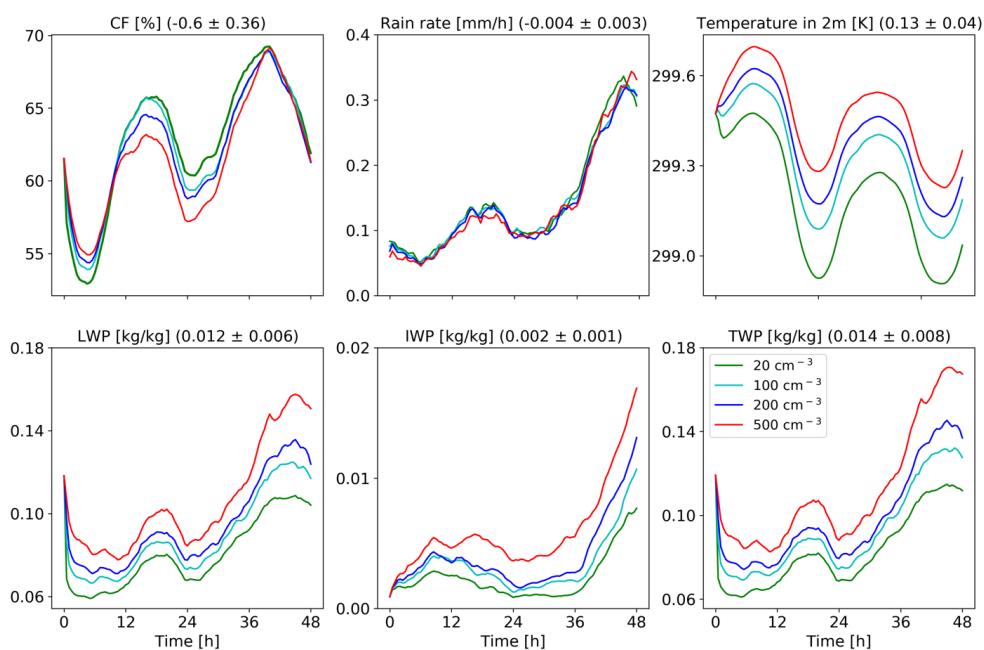
305 200 cm⁻³). Figure 8 demonstrates that the domain mean cloud fraction (CF) generally decreases
306 with the increase in CDNC (except for the first ~10 hours of the simulations). Examining the
307 vertical structure of the CF response (Fig. 9), demonstrates that with the increase in CDNC there
308 is a reduction in the low level (below 800 mb) CF concomitantly with an increase in CF at the
309 middle and upper troposphere. The differences in rain rate between the different simulations are
310 small. However, both the liquid water path (LWP) and the ice water path (IWP) show a consistent
311 increase with CDNC. Accordingly, also the total water path (TWP), which is the sum of the LWP
312 and the IWP, substantial increases with CDNC. The vertical profiles of the different hydrometers
313 (Fig. 9) indicate, as expected, that the cloud droplet mass mixing ration (q_c - droplet with radius
314 smaller than 40 μm) increases with CDNC, while the rain mass mixing ratio (q_r - drops with
315 radius larger than 40 μm) decreases due to the shift in the droplet size distribution to smaller
316 sizes under larger CDNC conditions. As this case is dominated by shallow clouds, there exists
317 only a comparably small amount of ice mixing ration (q_i) (c.f. Fig. 17), but its concentration
318 increases with the CDNC increase. The combined effect of the increase in CDNC is to
319 monotonically increase the total water mixing ratio (q_t) above 800 mb (Fig. 9). The relative
320 increase in q_t with CDNC becomes larger at higher levels.

321 The increase in cloud water with increasing CDNC can explain both the reductions in the net
322 downward SW fluxes (both at TOA and surface) and the decrease in outgoing LW flux at TOA
323 (Fig. 7), as it results in more SW reflection concomitantly with more LW trapping in the
324 atmosphere (Koren et al., 2010). Another contributor to the SW flux reduction (more reflectance)
325 at the TOA is the Twomey effect (Twomey, 1977), while, the decrease in the low-level CF
326 compensates some of this effect. Here we present the outcome of these contradicting effects on
327 the SW fluxes, which shows a reduction at both the TOA and surface (Fig. 7). For estimating the
328 relative contribution of the Twomey effect compare to the cloud adjustments (CF and TWP
329 effects) to the SW flux changes, we have re-run the simulations with the Twomey effect turned
330 off (the radiation calculations do not consider the changes in effective radius between the
331 different simulations). It demonstrates that without the Twomey effect the TOA SW difference
332 is only -1.7 W/m^2 as compared to -7.5 W/m^2 with the Twomey effect, demonstrating the
333 predominant role of the Twomey effect. For estimating the relative contribution of the changes
334 in CF and TWP to the SW flux changes we have conducted off-line radiative transfer sensitivity
335 tests. To quantify the TWP radiative effect we feed the same CF vertical profile from the model
336 into BUGSrad while allowing the TWP vertical profile to change (and visa versa to compute the



337 CF radiative effect). This approach demonstrates that the contribution from the small reduction
338 in CF is negligible compared to the increased SW reflectance caused by the increase in TWP.

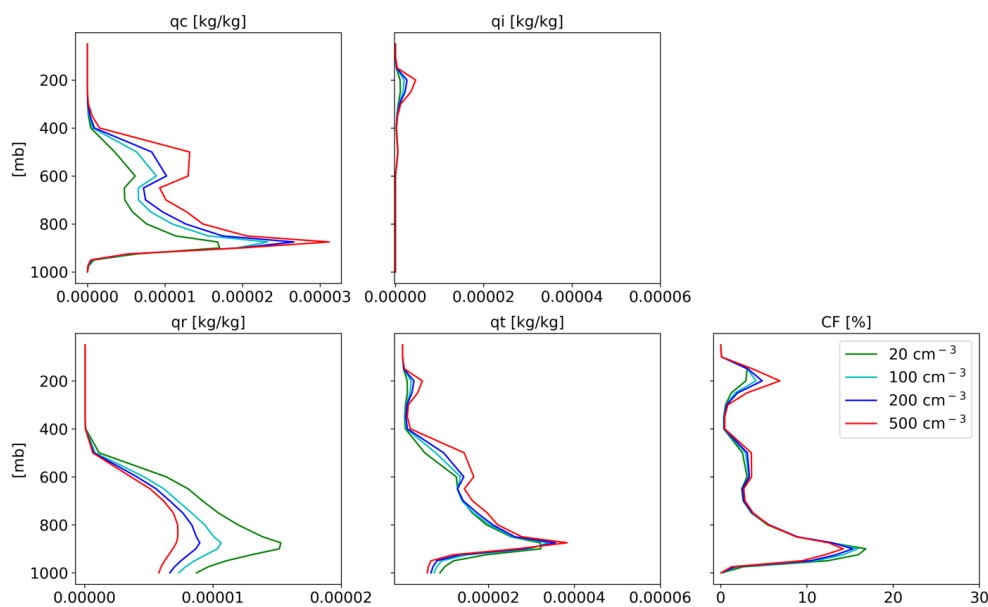
339 We also note a monotonic increase in the near surface temperature with CDNC (see also Fig. 10
340 below). This trend can be explained by warm rain suppression with increasing CDNC that leads
341 to less evaporative cooling (see the decrease in the total amount of water mass mixing ratio just
342 above the surface in Fig. 9, (Dagan et al., 2016; Albrecht, 1993; Seigel, 2014; Seifert and Heus,
343 2013; Lebo and Morrison, 2014)). In addition, it was shown that under polluted conditions the
344 rain drops below cloud base are larger, hence evaporating less efficiently (Lebo and Morrison,
345 2014; Dagan et al., 2016). The increase in the near surface temperature drives the decrease in the
346 Q_{SH} (Fig. 6).



347

348 **Figure 8. Domain average properties as a function of time for the different CDNC simulations for the shallow-**
349 **cloud dominated case. The properties that are presented here are: cloud fraction (CF), rain rate**
350 **in 2 m, liquid water path (LWP), ice water path (IWP) and total water path (TPW = LWP + IWP). For each**
351 **property the mean difference between all combinations of simulations, normalized to a factor 5 increase in**
352 **CDNC, and its standard deviation appear in parenthesis.**

353



354

355 **Figure 9.** Domain and time average vertical profiles for the different CDNC simulations for the shallow-cloud
356 dominated case. The properties that are presented here are: cloud droplet mass mixing ratio (q_c – for clouds’
357 droplets with radius smaller than $40\ \mu\text{m}$), ice mass mixing ratio (q_i), rain mass mixing ratio (q_r - for clouds’
358 drops with radius larger than $40\ \mu\text{m}$), total water mass mixing ratio ($q_t = q_c + q_i + q_r$), and cloud fraction (CF).
359 The x-axis ranges are identical as for the deep-cloud dominated case – Fig. 17.

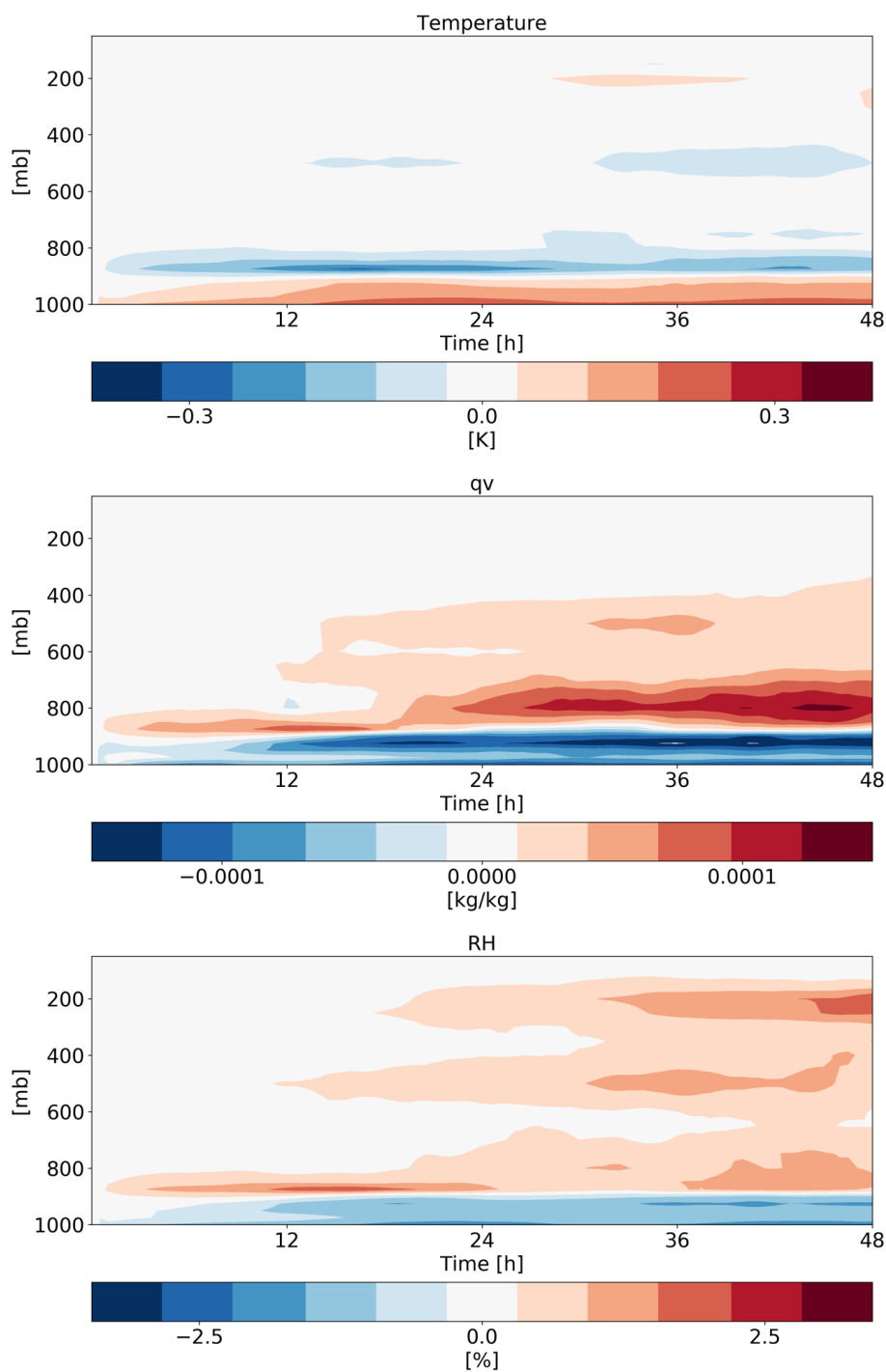
360

361 In addition to the clouds’ effect on the radiation fluxes, changes in humidity could also contribute
362 (Fig. 10). We note that increase in CDNC leads to increase in relative humidity (RH) and specific
363 humidity (q_v) at the middle and upper troposphere without a significant temperature change. The
364 increased humidity at the upper troposphere would act to decrease the outgoing LW flux, a
365 similar effect as the increased ice content at the upper troposphere has (Fig. 9). However,
366 sensitivity studies with off-line radiative transfer calculations using BUGSrad, demonstrate that
367 the vast majority of the different in F_{LW}^{TOA} between clean and polluted conditions emerges from
368 the cloudy skies (rather than clear-sky), suggesting that the effect of the increased ice content at
369 the upper troposphere predominant.

370 Both the increase in water vapor and ice content at the upper troposphere are driven by increase
371 in water (liquid and ice) mass flux with increasing CDNC to these levels (Fig. 11). The increase
372 in mass flux is driven partially by the small increase in vertical velocity (especially for updraft



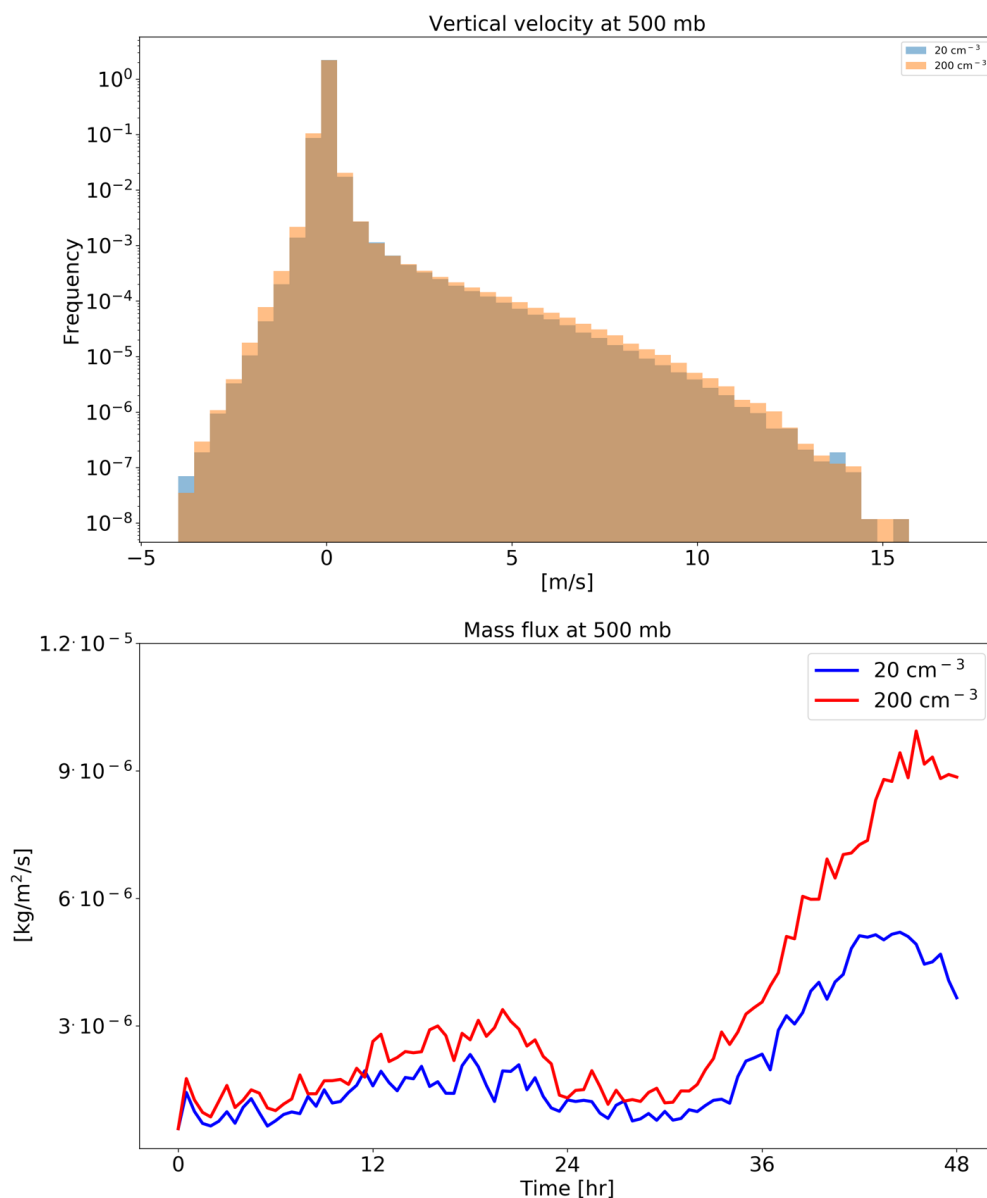
373 between 5 and 10 m/s) and mostly due to the larger water mass mixing ratio (Fig. 9) that leads
374 to an increase in mass flux even for a given vertical velocity. The increased relative humidity at
375 the upper troposphere, further increases the ice particle lifetime at these levels (in addition to the
376 microphysical effect (Grabowski and Morrison, 2016)) as the evaporation rate decreases. In
377 addition, the differences in the thermodynamics evolution between the different simulations (Fig.
378 10) demonstrate drying and warming of the boundary layer with increasing CDNC, due to
379 reduction in rain evaporation below cloud base and deepening of the boundary layer (Dagan et
380 al., 2016; Lebo and Morrison, 2014; Seifert et al., 2015; Spill et al., 2019). The drying of the
381 boundary layer could explain the reduction in the low cloud fraction (Fig. 9 (Seifert et al., 2015)).





383 **Figure 10. Hovmöller diagrams of the differences in the domain mean temperature, specific humidity (q_v)**
384 **and relative humidity (RH) vertical profiles between polluted (CDNC = 200 cm^{-3}) and clean (CDNC = 20 cm^{-3})**
385 **3) simulations for the shallow-cloud dominated case (10-12/08/2016).**

386



387

388 **Figure 11. histograms of ICON simulated vertical velocity at the level of 500 mb (upper), and the time**
389 **evolution of the net upwards water (liquid and ice) mass flux (lower) for a clean (CDNC = 20 cm^{-3}) and**

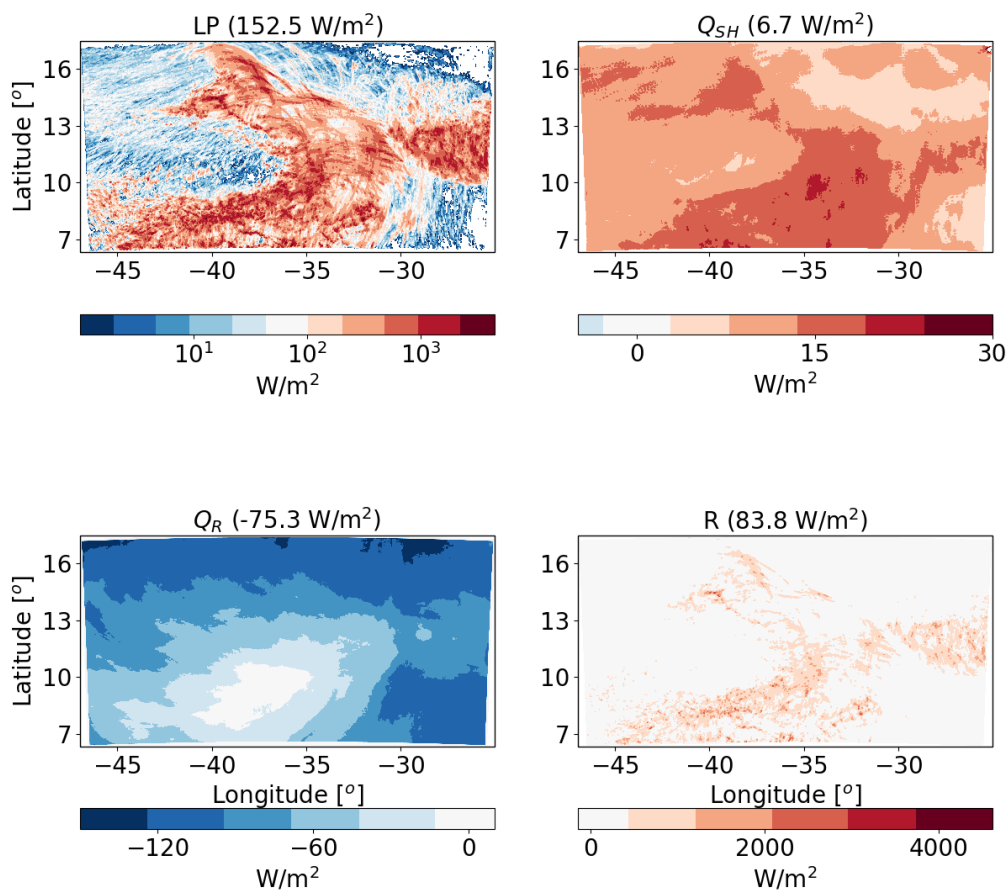


390 **polluted (CDNC = 200 cm⁻³) simulations for the shallow-cloud dominated case (10-12/08/2016). The 500 mb**
391 **level is chosen as it represents the transition between the warm part to the cold part of the clouds.**

392

393 **Deep-cloud dominated case -16-18/08/2016**

394 Next, we analyse the atmospheric energy budget for the deep-cloud dominated case (Fiona
395 tropical storm – Fig. 12). As opposed to the shallow-cloud dominated case, in this case the *LP*
396 contribution dominates over the radiative cooling and hence the residual *R* is positive and large.
397 This difference in the base line atmospheric energy budget between the different cases simulated
398 here, enable an examination of the aerosol effect on the atmospheric energy budget under
399 contrasting initial conditions. As in the shallow-cloud dominated case, the *Q_R* values varies
400 between small values (especially at the regions that were mostly covered by deep clouds) to
401 larger negative values (dominated at the regions that were covered by shallow clouds). The *Q_{SH}* is
402 positive and an order of magnitude smaller than the *Q_R* and *LP*, similar to the shallow-cloud
403 dominated case.



404

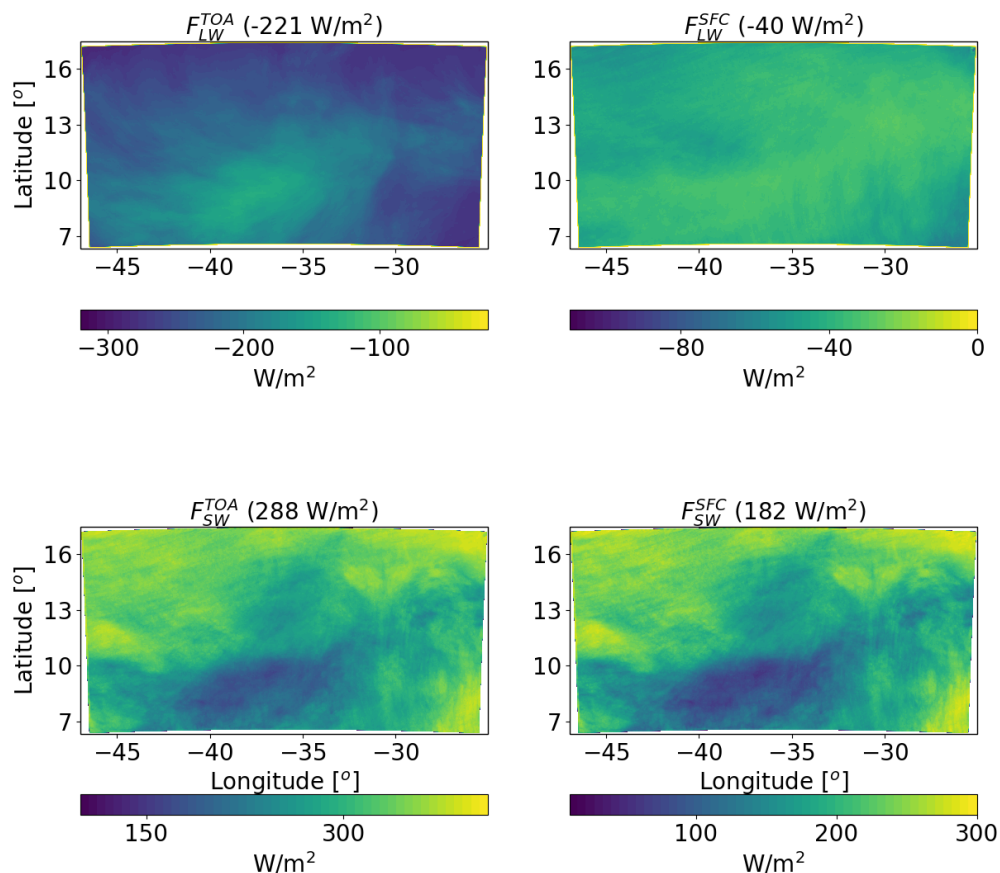
405 **Figure 12.** Spatial distribution of the time mean of the different terms of the energy budget for the ICON
406 simulation of the deep-cloud dominated case (16-18/08/2016) with $CDNC = 20 \text{ cm}^{-3}$. The terms that appear
407 here are: LP - latent heat by precipitation, Q_{SH} - sensible heat flux, Q_R - atmospheric radiative warming, and
408 R - the residual. The domain and time-mean value of each term appears in parenthesis.

409

410 Further examination of the radiative fluxes (Fig. 13) demonstrates again the resemblance in the
411 spatial structure between Q_R and F_{LW}^{TOA} . As compared to the shallow-cloud dominated case, since
412 the clouds are more opaque and cover larger fraction of the sky, there is a decrease in the
413 magnitude of all fluxes (in different amount). For example, F_{SW}^{FC} is lower by 41 W/m^2
414 (representing larger SW reflectance back to space) and the magnitude of F_{LW}^{TOA} by 47 W/m^2 as
415 compare to the shallow-cloud dominated case. The combined effect of the radiative flux



416 differences between the two cases is a decrease of the atmospheric radiative cooling by 39.6
417 W/m^2 (-114.7 compare with -75.3 W/m^2 – see Figs. 5 and 13).



418

419 **Figure 13. Spatial distribution of ICON simulated time-mean longwave (LW) and shortwave (SW) radiation**
420 **fluxes at the top of atmosphere (TOA) and surface (SFC) for a simulation of the deep-cloud dominated case**
421 **(16-18/08/2016) with $\text{CDNC} = 20 \text{ cm}^{-3}$. The domain and time mean value of each term appears in parenthesis.**

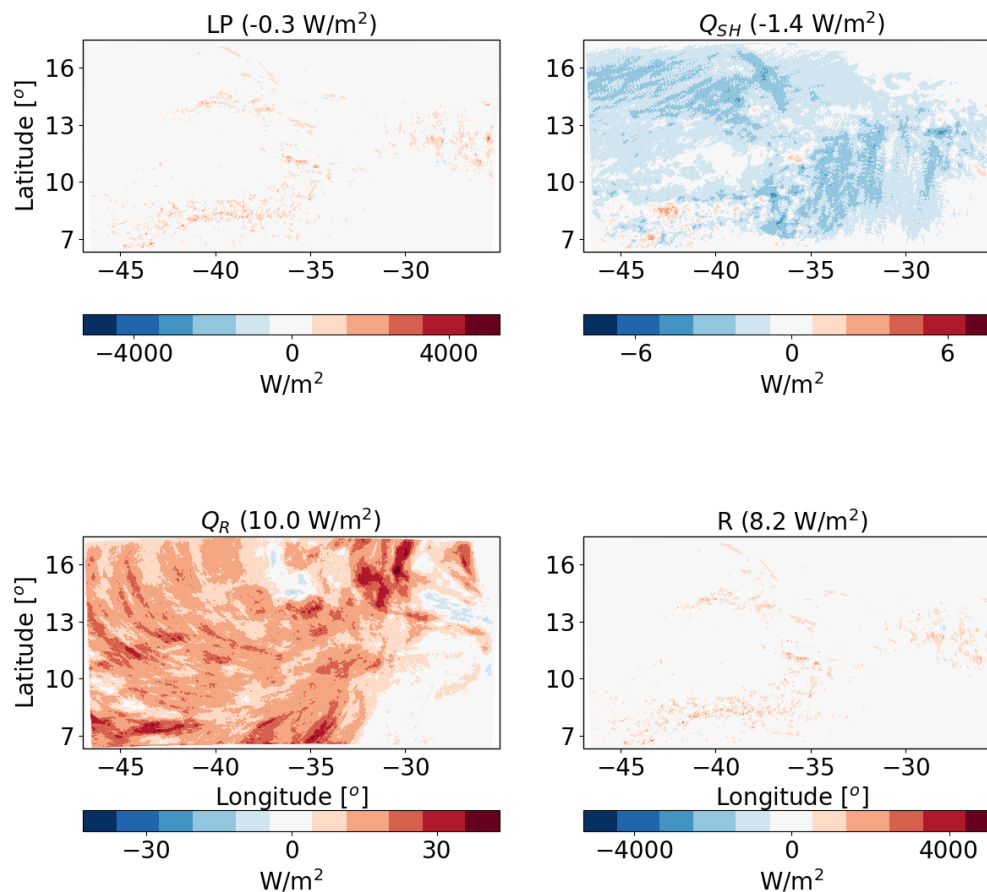
422

423 **Response to aerosol perturbation – deep-cloud dominated case**

424 For the deep-cloud dominated case, an increase in CDNC results in a decrease in LP by -0.3
425 W/m^2 . Again, this difference is due to non-statistically significant precipitation changes (see also
426 Fig. 16 below). A similar Q_{SH} decrease as in the shallow-cloud dominated case is observed in the
427 deep-clouds dominated case (see Figs. 14 and 6). The predominant difference in the response



428 between the two cases is in Q_R , which increases much more in the deep-cloud dominated case:
429 10.0 W/m^2 (Fig. 14) compared with 1.6 W/m^2 in the shallow-cloud dominated case (Fig. 6).



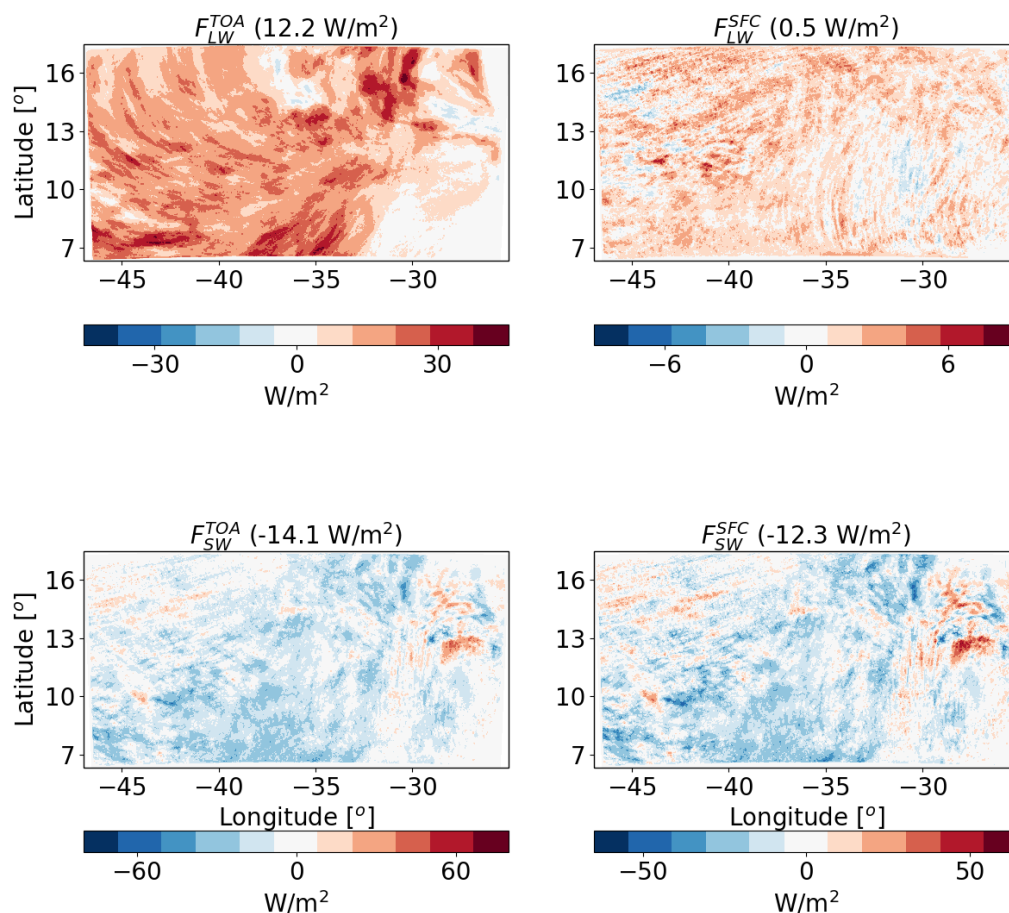
430
431 **Figure 14.** The differences between polluted ($\text{CDNC} = 200 \text{ cm}^{-3}$) and clean ($\text{CDNC} = 20 \text{ cm}^{-3}$) ICON
432 simulations of the time-mean terms of the energy budget for the deep-cloud dominated case (16-18/08/2016).
433 The terms that appears here are: LP - latent heat by precipitation, Q_{SH} - sensible heat flux, Q_R - atmospheric
434 radiative warming, and R - the residual. The domain and time mean value of each term appears in
435 parenthesis.

436

437 The large increase in Q_R is caused mostly by the increase in F_{LW}^{TOA} (which becomes less negative
438 i.e. less outgoing LW radiation under polluted conditions – Fig. 15). The CDNC effect on F_{LW}^{SEC}
439 has a much smaller magnitude. The SW fluxes changes are substantial (-14.1 W/m^2 at TOA and
440 -12.3 W/m^2 at the surface), however, in terms of the atmospheric energy budget, since clouds do



441 not absorb much in the SW, the TOA and surface changes almost cancel each other out and the
442 net effect is only $\sim 1.8 \text{ W/m}^2$ atmospheric radiative cooling (which decrease some of the LW
443 warming). The net TOA total (SW+LW) radiative flux change is about -1.9 W/m^2 . The trends in
444 the mean cloud properties (Figs. 16 and 17 below) can explain this large radiative response.



445

446 **Figure 15.** The differences between polluted ($\text{CDNC} = 200 \text{ cm}^{-3}$) and clean ($\text{CDNC} = 20 \text{ cm}^{-3}$) ICON
447 simulations of the time mean radiative longwave (LW) and shortwave (SW) fluxes at the top of atmosphere
448 (TOA) and surface (SFC) for the deep-cloud dominated case (16-18/08/2016). The domain and time mean
449 value of each term appears in parenthesis.

450

451 Figure 16 presents some of the domain mean properties as a function of time for the deep-cloud
452 dominated case. It demonstrates an increase in CF with CDNC which is more significant during



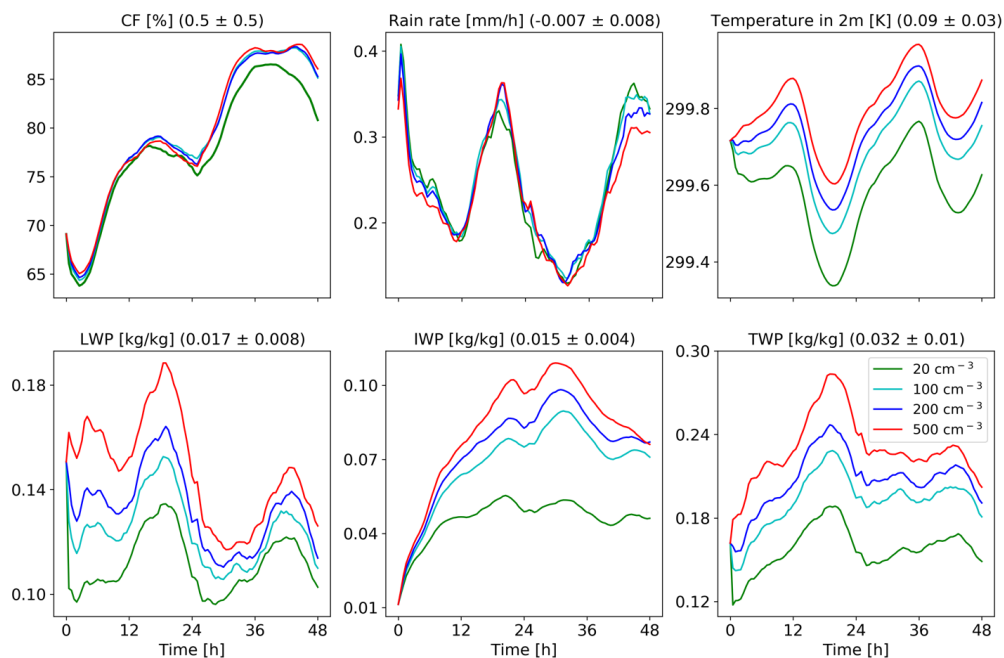
453 the second day of the simulation. This is opposite to the CF reduction in the shallow-cloud
454 dominated case (Fig. 8). It also demonstrates a very significant increase in LWP and, even more
455 (in relative terms), in IWP and thus also in TWP. The increase in CF and water content can
456 explain the decrease in SW fluxes both at TOA and surface (Fig. 15) as more SW is being
457 reflected back to space. The larger SW reflection under increased CDNC is also contributed to
458 by the Twomey effect (Twomey, 1977). Re-running the simulations without the Twomey effect
459 result in 9.6 W/m² reduction in the TOA SW flux as compare to 14.1 W/m² with the Twomey
460 effect on. We note that the relative role of the Twomey effect (compare to the cloud adjustments
461 – CF and TWP) is larger in the shallow-cloud dominated case as compare to the deep-cloud
462 dominated case (-9.6 W/m² and -14.1 W/m² for simulations with and without the Twomey effect
463 in the deep-cloud dominated case, compare to -1.7 W/m² and -7.5 W/m² in the shallow-cloud
464 dominated case, respectively). However, it should be noted that the Twomey effect due to
465 changes in the ice particles size distribution was not considered. In this case, unlike in the
466 shallow-cloud dominated case, the three contributions to the SW changes (CF, Twomey and
467 LWP/IWP, e.g. (Goren and Rosenfeld, 2014)) all contribute to the SW flux reduction (Fig. 15
468 presents the results of all contributors). Off-line sensitivity tests demonstrate that the relative
469 contribution of the TWP and the CF to the increase in SW reflectance is roughly $\frac{3}{4}$ and $\frac{1}{4}$,
470 respectively.

471 The vertical profile changes with CDNC (Fig. 17) demonstrate a consistent picture of a decrease
472 in CF in low clouds and a significant increase in CF and liquid and ice content at the mid and
473 upper troposphere. The CF increase at the upper troposphere, and especially the increase in the
474 ice content, can explain the decrease in the outgoing LW radiation (Fig. 15). The increase in ice
475 content at the upper troposphere is in agreement with recent observational studies (Gryspeerdt et
476 al., 2018; Sourdeval et al., 2018; Christensen et al., 2016). Analysis of the upward water mass
477 flux from the warm to the cold part of the clouds (at 500 mb) in the different simulations (Fig.
478 19), demonstrates a substantial increase with the increase in CDNC (Chen et al., 2017), which
479 occur even without a large change in the vertical velocity due to the increase in the water content
480 (Fig. 17) and the delay in the rain formation to higher levels (Heikenfeld et al., 2019). Similar to
481 the shallow-cloud dominated case (Fig. 8), the near surface temperature monotonically increases
482 with CDNC, while the effect on the mean rain rate is small.

483 The differences in the thermodynamic evolution between polluted and clean conditions for this
484 case (Fig. 18), demonstrate the same trend as in the shallow-cloud dominated case (Fig. 10).
485 Here again, we note an increase in the humidity at the mid and upper troposphere, that contribute

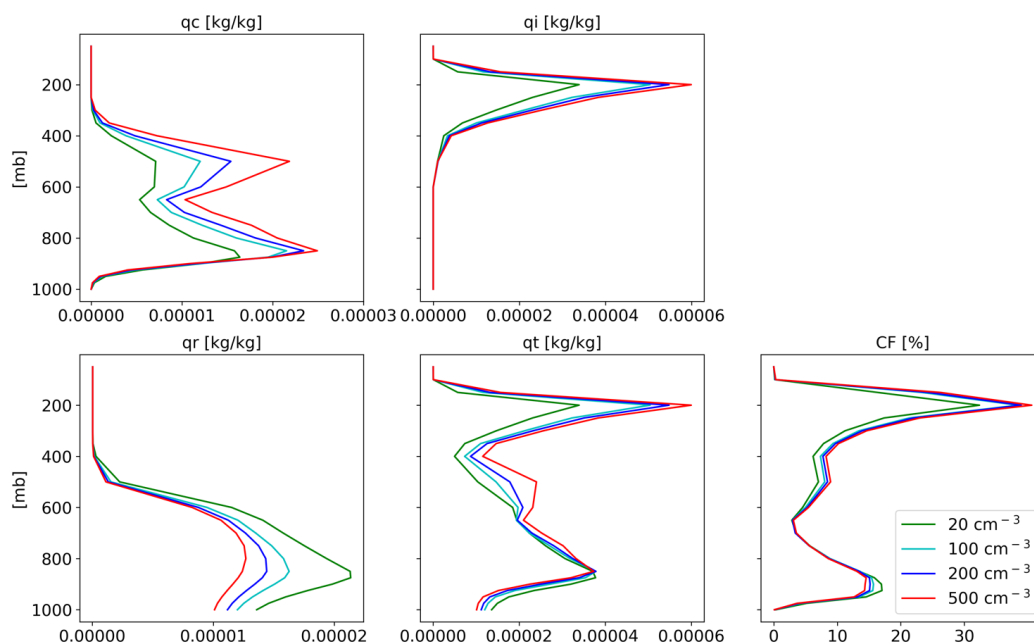


486 to the reduction in the outgoing LW flux. The deepening, drying and warming of the boundary
487 layer are observed in this case as well. Both the increase in humidity at the mid-upper troposphere
488 and the deepening of the boundary layer (Seifert et al., 2015) could cause a reduction of the
489 outgoing LW flux. To distinguished the effect of clouds and humidity at the different levels on
490 the outgoing LW flux, we have conducted sensitivity off-line radiative transfer calculations using
491 BUGSrad. As in the shallow-cloud dominated case, the difference in outgoing LW flux between
492 clean and polluted conditions primarily emerges from the CDNC effect on clouds. The small
493 remaining effect of the clear sky ($\sim 0.2 \text{ W/m}^2$) is contributed by the change in the humidity at the
494 mid and upper troposphere rather than by the deepening of the boundary layer (which would lead
495 to LW emission from lower temperatures and is expected to be more significant under lower free
496 troposphere humidity conditions).



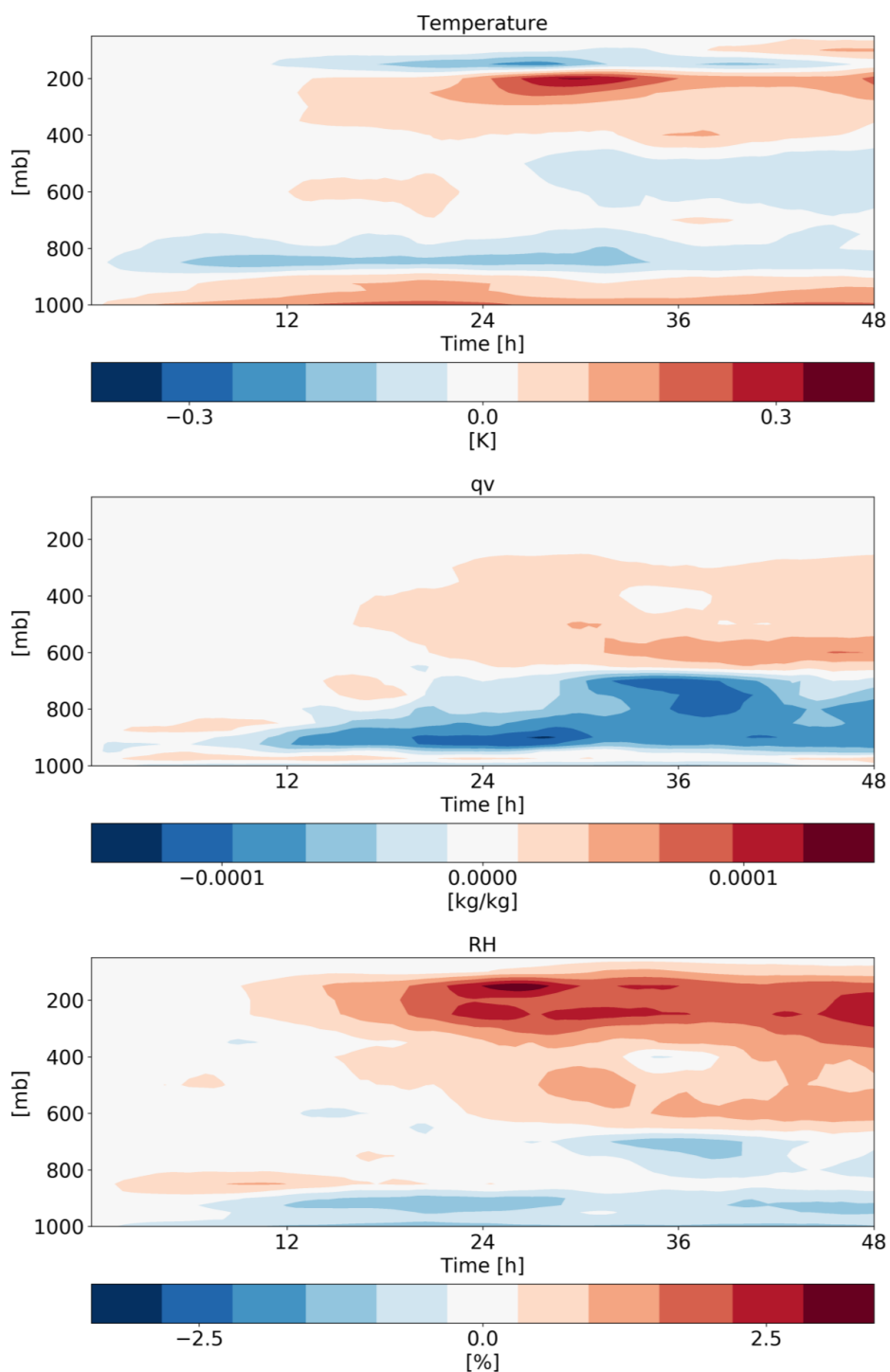
497
498 **Figure 16. Domain average properties as a function of time for the different CDNC simulations for the deep-**
499 **cloud dominated case. The properties that are presented here are: cloud fraction (CF), rain rate**
500 **in 2 m, liquid water path (LWP), ice water path (IWP) and total water path (TPW = LWP + IWP). For each**
501 **property the mean difference between all combinations of simulations, normalized to a factor 5 increase in**
502 **CDNC, and its standard deviation appear in parenthesis.**

503



504

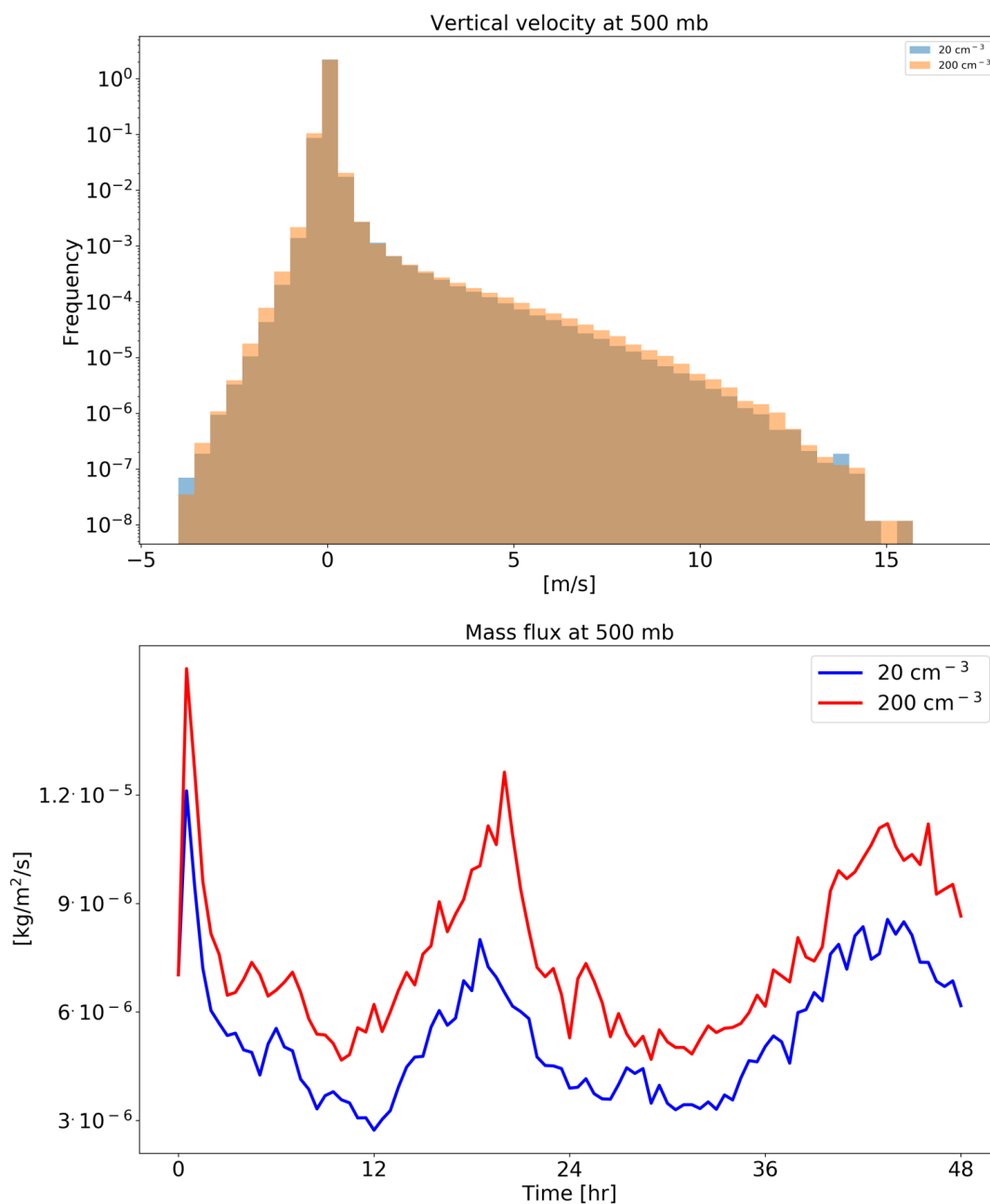
505 **Figure 17.** Domain and time average vertical profiles for the different CDNC simulations for the shallow-
506 cloud dominated case. The properties that are presented here are: cloud droplet mass mixing ratio (q_c – for
507 clouds’ droplets with radius smaller than $40\ \mu\text{m}$), ice mass mixing ratio (q_i), rain mass mixing ratio (q_r - for
508 clouds’ drops with radius larger than $40\ \mu\text{m}$), total water mass mixing ratio ($q_t = q_c + q_i + q_r$), and cloud
509 fraction (CF).





511 **Figure 18.** Hovmöller diagrams of the differences in the domain mean temperature, specific humidity (q_v)
512 and relative humidity (RH) vertical profiles between polluted (CDNC = 200 cm^{-3}) and clean (CDNC = 20 cm^{-3})
513 simulations for the deep-cloud dominated case (16-18/08/2016).

514



515



516 **Figure 19. histograms of ICON simulated vertical velocity at the level of 500 mb (upper), and the time**
517 **evolution of the net upwards water (liquid and ice) mass flux (lower) for a clean (CDNC = 20 cm⁻³) and**
518 **polluted (CDNC = 200 cm⁻³) simulations for the deep-cloud dominated case (16-18/08/2016). The 500 mb level**
519 **is chosen as it represents the transition between the warm part to the cold part of the clouds.**

520

521 Summary and conclusions

522 Two different case studies of tropical cloud systems over the Atlantic Ocean were simulated
523 using the ICON numerical model in a cloud resolving configuration with 1.2 km resolution and
524 a relatively large domain (~22° x 11°). The cases represent dates from the NARVAL 2 field
525 campaign that took place during August 2016 and have different dominant cloud types and
526 different dominating terms in their energy budget. The first case (10-12/8/2016) is shallow-cloud
527 dominated and hence dominated by radiative cooling, while the second case (16-18/8/2016) is
528 dominated by deep convective clouds and hence dominated by precipitation warming. The main
529 objective of this study is to analyse the response of the atmospheric energy budget to changes in
530 cloud droplet number concentration (CDNC), which serve as a proxy for (or idealized
531 representation of) changes in aerosol concentration. This enables better understanding of the
532 processes acting in global-scale studies trying to constrain aerosol effect on precipitation changes
533 using the energy budget perspective (O’Gorman et al., 2012;Muller and O’Gorman,
534 2011;Hodnebrog et al., 2016;Samset et al., 2016;Myhre et al., 2017;Liu et al., 2018;Richardson
535 et al., 2018;Dagan et al., 2019a). Our results demonstrate that regional atmospheric energy
536 budgets can be significantly perturbed by changes in CDNC and that the magnitude of the effect
537 is cloud regime dependent (even for a given geographical region and given time of the year as
538 the two cases are separated by less than a week).

539 Figure 20 summarizes the energy and radiation response of the two simulated cases to CDNC
540 perturbations. It shows that the atmosphere in the deep-cloud dominated case experiences a very
541 strong atmospheric warming due to an increase in CDNC (10.0 W/m²). Most of this warming is
542 caused by a reduction in the outgoing LW radiation at the TOA. The SW radiative fluxes (both
543 at the TOA and surface) is also significantly modified but their net effect on the atmospheric
544 column energy budget is small. The net TOA radiative fluxes change in this case is -1.9 W/m².
545 Beside the atmospheric radiative warming, changes in precipitation (~-0.3 W/m²), and in sensible
546 heat flux (Q_{SH} , -1.4 W/m²) also contribute to the total trend as a response of increase in CDNC.
547 We note that since 1 mm/hr of rain is equivalent to 628 W/m², even negligible changes in



548 precipitation of less than 0.5 mm over 48 hr (as seen in our simulations) can still appear as
549 significant changes in the atmospheric energy budget and contribute a few W/m^2 .

550 The response of the radiative fluxes can be explained by the changes in the mean cloud and
551 thermodynamic properties in the domain. The mean cloud fraction (CF) increases with the
552 increase in CDNC (Fig. 16) while the vertical structure of it indicates a reduction in the low
553 cloud fraction (below 800 mb) and an increase in the mid and upper troposphere CF (Fig. 17).
554 The water content (both liquid and ice) also increase with the increase in CDNC (Figs. 16 and
555 17) with increasing amount with height. These changes in the mean cloud properties drive both
556 the reduction in SW fluxes at TOA and surface and LW flux at TOA as the clouds become more
557 opaque (Koren et al., 2010; Storelvmo et al., 2011) and cover a larger fraction of the sky. In
558 addition to cloud responses, the domain-mean thermodynamic conditions change as well (Fig.
559 18). Specifically, the humidity content at the mid and upper troposphere increases with higher
560 CDNC, (due to increase mass flux to the upper troposphere) which further decreases the outgoing
561 LW flux at the TOA. However, the vast majority of the LW effect emerges from the changes in
562 clouds.

563 Both the increase in water vapor and ice content at the upper troposphere are driven by an
564 increase in water mass flux with increasing CDNC to these levels (Fig. 19, (Koren et al., 2005;
565 Rosenfeld et al., 2008; Altaratz et al., 2014; Chen et al., 2017)), which is caused mostly by the
566 increase in the water mixing ratio at the mid-troposphere rather than by increase in vertical
567 velocity (Figs. 11 and 19). The ice content at the upper troposphere is also increased due to
568 reduction in the ice falling speed (Grabowski and Morrison, 2016), while the increased relative
569 humidity at these levels, further increases the ice particle lifetime due to slower evaporation.
570 However, the increase in water mass flux to the upper layers is not accompanied with an increase
571 in precipitation as predicted by the classical “invigoration” paradigm (Altaratz et al., 2014;
572 Rosenfeld et al., 2008), which suggest that some compensating mechanisms are operating
573 (Stevens and Feingold, 2009).

574 In the shallow-cloud dominated case (which also contains a significant amount of deep
575 convection), the response of Q_R is weaker but still substantial (a total decrease in the atmospheric
576 radiative cooling of 1.6 W/m^2 - Fig. 20). Here again, the changes in Q_{SH} decrease about -1.4
577 W/m^2 of this atmospheric warming. As in the deep-cloud dominated case, most of the
578 atmospheric radiative warming is caused by reduction in the outgoing LW flux, while the surface
579 and TOA SW fluxes changes are non-negligible but cancel each other out (in terms of the



580 atmospheric energy budget – reflecting small SW atmospheric absorption changes). However, a
581 significant TOA net (SW+LW) radiative flux change of ~ -5.2 W/m² remains. In this case, the
582 cloud-mean effect on radiation is more complicated. While CF decreases with increasing CDNC,
583 the mean water path (both LWP and IWP) increases (Fig. 8). As in the deep-cloud dominated
584 case, the increase in the water content occurs mostly at the mid and upper troposphere, while the
585 decrease in CF occurs mostly in the lower troposphere (Fig. 9). In terms of the SW fluxes, the
586 effect of the decrease in low CF (decrease SW reflections) and the increase in water mass
587 (increase SW reflections) would partially compensate, while the Twomey effect (Twomey, 1977)
588 adds to the increase SW reflections. In this case, the net effect is more SW reflected back to
589 space at TOA and a net negative flux change (including also the LW).

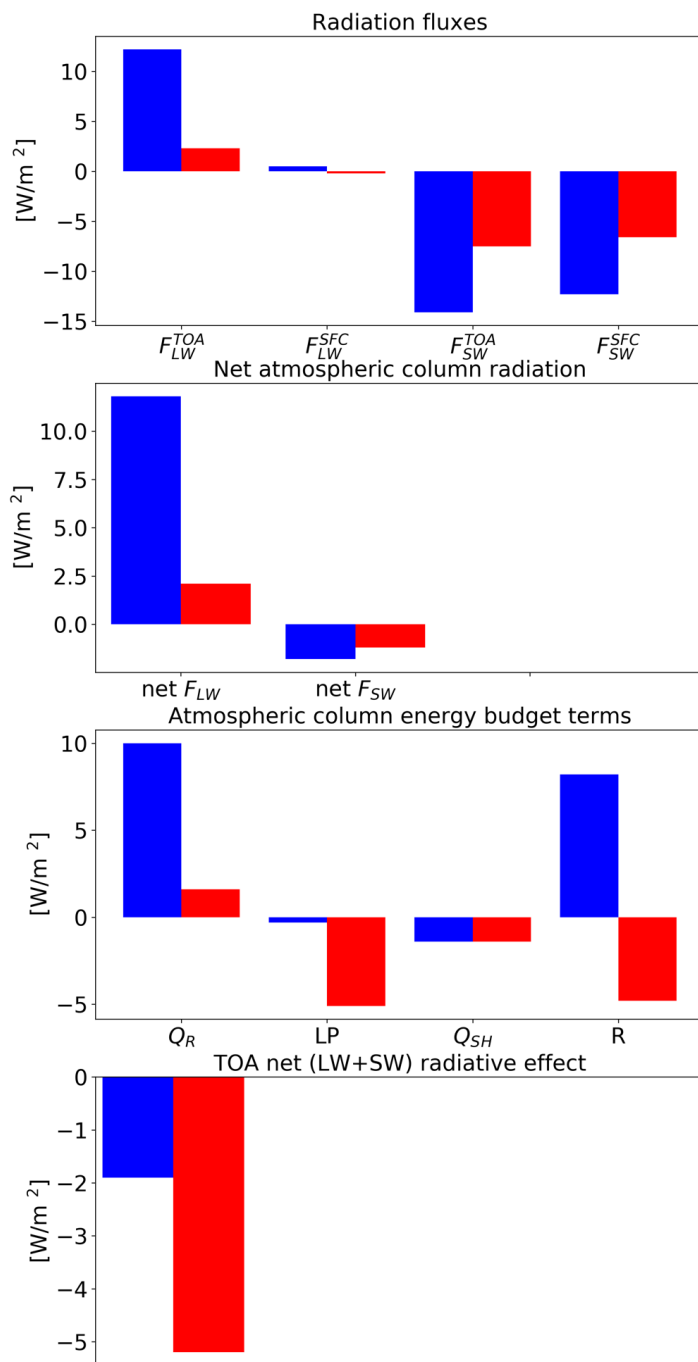
590 There exists a large spread in estimates of aerosol effects on clouds for different cloud types and
591 different environmental conditions. In this study, as we use a relatively large domain (22° x 11°)
592 and two different dates (each for two days), we sample many different local environmental
593 conditions and cloud types. Such more realistic setups (although with lower spatial resolution)
594 could provide more reliable estimates of aerosol effects on heterogeneous cloud systems than
595 just one-cloud-type, small domain simulations (as was done in many previous studies, e.g (Dagan
596 et al., 2017; Seifert et al., 2015; Ovchinnikov et al., 2014)). In addition, the realistic setup with
597 the continuously changing boundary conditions and systems that pass through the domain
598 prevent conclusions that might be valid only in cyclic double periodic large eddy simulations, as
599 the background meteorological conditions change more realistically (Dagan et al., 2018b).
600 Another uncertainty in the assessment of the aerosol response are the large differences between
601 different models and microphysical schemes (White et al., 2017; Fan et al., 2016; Khain et al.,
602 2015; Heikenfeld et al., 2019). In this study, as we use only one model, we do not address this
603 uncertainty. In future work we intend to examine the response in multiple models. In addition,
604 more detailed observational constraints on the models are needed. Furthermore, we do not
605 include temporal evolution of the aerosol concentration. Feedbacks between the aerosol
606 concentration and clouds processes (such as wet scavenging) would add another layer of
607 complexity that should be accounted for in future work.

608 Generally, the global mean aerosol radiative forcing is estimated to be negative (Boucher et al.,
609 2013; Bellouin et al., 2019). However, these global aerosol forcing estimates have so far not
610 included the radiative forcing associated with potential effects of aerosols on deep convection –
611 and these effects are not represented in most current climate models due to limitations in
612 convection parameterisations, with only a few exceptions (Kipling et al., 2017; Labbouz et al.,



613 2018). Here we demonstrate the existence of non-negligible aerosol radiative effects (of -5.2 and
614 -1.9 W/m² for the shallow and deep cloud dominated cases, respectively) in tropical cloud
615 systems, that contained both deep and shallow convective clouds, with significant SW and LW
616 contributions. From the (limited) two cases simulated here, it appears that (in agreement with
617 previous studies) the aerosol effect may be regime dependent and that even within a given cloud
618 regime the effect may vary with the meteorological conditions.

619 Finally, we hypothesise that the aerosol impact shown on the atmospheric energy balance, with
620 increasing divergence of dry static energy from deep convective regions concomitantly with
621 increased convergence in shallow clouds regions, can have effects on the large-scale circulation.
622 This should be investigated in future work.



623

624 **Figure 20. Summary of the radiation and energy response to CDNC perturbation in the two different cases.**
 625 **Blue represent the deep-cloud dominated case while red the shallow-cloud.**



626 **Author contributions.** G. D. carried out the simulations and analyses presented. G.C., D.K. and
627 A.S. assisted with the simulations. M.C. assisted with the radiative transfer calculations and
628 comparison with observations. P. S. and A.S. assisted with the design and interpretation of the
629 analyses. G. D. prepared the manuscript with contributions from all co-authors.

630 **Acknowledgements:**

631 This research was supported by the European Research Council (ERC) project constRaining
632 the EffeCts of Aerosols on Precipitation (RECAP) under the European Union's Horizon 2020
633 research and innovation programme with grant agreement No 724602. The simulations were
634 performed using the ARCHER UK National Supercomputing Service. ECMWF is
635 acknowledged for providing Era-interim data set (<https://apps.ecmwf.int/datasets/>). We
636 acknowledge MPI, DWD and DKRZ for the NARVAL simulations.

637

638 **References**

- 639 Albrecht, B. A.: Aerosols, cloud microphysics, and fractional cloudiness, *Science* (New York, NY), 245,
640 1227, DOI: 10.1126/science.245.4923.1227, 1989.
- 641 Albrecht, B. A.: Effects of precipitation on the thermodynamic structure of the trade wind boundary
642 layer, *Journal of Geophysical Research: Atmospheres* (1984–2012), 98, 7327-7337,
643 <https://doi.org/10.1029/93JD00027>, 1993.
- 644 Altaratz, O., Koren, I., Remer, L., and Hirsch, E.: Review: Cloud invigoration by aerosols—Coupling
645 between microphysics and dynamics, *Atmospheric Research*, 140, 38-60,
646 <https://doi.org/10.1016/j.atmosres.2014.01.009>, 2014.
- 647 Aminou, D.: MSG's SEVIRI instrument, *ESA Bulletin* (0376-4265), 15-17, 2002.
- 648 Andreae, M. O., Rosenfeld, D., Artaxo, P., Costa, A. A., Frank, G. P., Longo, K. M., and Silva-Dias, M. A.
649 F.: Smoking rain clouds over the Amazon, *Science*, 303, 1337-1342, 10.1126/science.1092779, 2004.
- 650 Andreae, M. O.: Correlation between cloud condensation nuclei concentration and aerosol optical
651 thickness in remote and polluted regions, *Atmospheric Chemistry and Physics*, 9.2, 543-556, 2009.
- 652 Arakawa, A., and Schubert, W. H.: Interaction of a cumulus cloud ensemble with the large-scale
653 environment, Part I, *Journal of the Atmospheric Sciences*, 31, 674-701, 1974.
- 654 Bellouin, N., Quaas, J., Gryspeerdt, E., Kinne, S., Stier, P., Watson-Parris, D., Boucher, O., Carslaw, K.,
655 Christensen, M., and Daniau, A.-L.: Bounding aerosol radiative forcing of climate change, *Reviews of
656 Geophysics*, <http://hdl.handle.net/21.11116/0000-0003-9D8D-E>, 2019.
- 657 Boucher, O., Randall, D., Artaxo, P., Bretherton, C., Feingold, G., Forster, P., Kerminen, V., Kondo, Y.,
658 Liao, H., and Lohmann, U.: Clouds and aerosols, *Climate Change*, 571-657, 2013.
- 659 Chen, Q., Koren, I., Altaratz, O., Heiblum, R. H., Dagan, G., and Pinto, L.: How do changes in warm-
660 phase microphysics affect deep convective clouds?, *Atmospheric Chemistry and Physics*, 17, 9585-
661 9598, <https://doi.org/10.5194/acp-17-9585-2017>, 2017.
- 662 Christensen, M. W., Chen, Y. C., and Stephens, G. L.: Aerosol indirect effect dictated by liquid clouds,
663 *Journal of Geophysical Research: Atmospheres*, 121, <https://doi.org/10.1002/2016JD025245>, 2016.



- 664 Clough, S., Shephard, M., Mlawer, E., Delamere, J., Iacono, M., Cady-Pereira, K., Boukabara, S., and
665 Brown, P.: Atmospheric radiative transfer modeling: a summary of the AER codes, *Journal of*
666 *Quantitative Spectroscopy and Radiative Transfer*, 91, 233-244,
667 <https://doi.org/10.1016/j.jqsrt.2004.05.058>, 2005.
- 668 Costantino, L., and Bréon, F.-M.: Aerosol indirect effect on warm clouds over South-East Atlantic,
669 from co-located MODIS and CALIPSO observations, *Atmospheric Chemistry and Physics*, 13, 69-88,
670 2013.
- 671 Dagan, G., Koren, I., and Altaratz, O.: Aerosol effects on the timing of warm rain processes,
672 *Geophysical Research Letters*, 42, 4590-4598, [10.1002/2015GL063839](https://doi.org/10.1002/2015GL063839), 2015a.
- 673 Dagan, G., Koren, I., and Altaratz, O.: Competition between core and periphery-based processes in
674 warm convective clouds—from invigoration to suppression, *Atmospheric Chemistry and Physics*, 15,
675 2749-2760, <https://doi.org/10.5194/acp-15-2749-2015>, 2015b.
- 676 Dagan, G., and Chemke, R.: The effect of subtropical aerosol loading on equatorial precipitation,
677 *Geophysical Research Letters*, 43, <https://doi.org/10.1002/2016GL071206>, 2016.
- 678 Dagan, G., Koren, I., Altaratz, O., and Heiblum, R. H.: Aerosol effect on the evolution of the
679 thermodynamic properties of warm convective cloud fields, *Scientific Reports*, 6, 38769, DOI:
680 [10.1038/srep38769](https://doi.org/10.1038/srep38769), 2016.
- 681 Dagan, G., Koren, I., Altaratz, O., and Heiblum, R. H.: Time-dependent, non-monotonic response of
682 warm convective cloud fields to changes in aerosol loading, *Atmos. Chem. Phys.*, 17, 7435-7444,
683 [10.5194/acp-17-7435-2017](https://doi.org/10.5194/acp-17-7435-2017), 2017.
- 684 Dagan, G., Koren, I., and Altaratz, O.: Quantifying the effect of aerosol on vertical velocity and
685 effective terminal velocity in warm convective clouds, *Atmospheric Chemistry and Physics*, 18, 6761-
686 6769, <https://doi.org/10.5194/acp-18-6761-2018>, 2018a.
- 687 Dagan, G., Koren, I., Altaratz, O., and Lehahn, Y.: Shallow convective cloud field lifetime as a key
688 factor for evaluating aerosol effects, *iScience*, 10, 192-202,
689 <https://doi.org/10.1016/j.isci.2018.11.032>, 2018b.
- 690 Dagan, G., Koren, I., Kostinski, A., and Altaratz, O.: Organization and oscillations in simulated shallow
691 convective clouds, *Journal of Advances in Modeling Earth Systems*,
692 <https://doi.org/10.1029/2018MS001416>, 2018c.
- 693 Dagan, G., Stier, P., and Watson-Parris, D.: Contrasting response of precipitation to aerosol
694 perturbation in the tropics and extra-tropics explained by energy budget considerations, *Geophysical*
695 *Research Letters*, <https://doi.org/10.1029/2019GL083479>, 2019a.
- 696 Dagan, G., Stier, P., and Watson-Parris, D.: Analysis of the atmospheric water budget for elucidating
697 the spatial scale of precipitation changes under climate change, *Geophysical Research Letters*,
698 <https://doi.org/10.1029/2019GL084173>, 2019b
- 699 Dee, D., Uppala, S., Simmons, A., Berrisford, P., Poli, P., Kobayashi, S., Andrae, U., Balmaseda, M.,
700 Balsamo, G., and Bauer, P.: The ERA-Interim reanalysis: Configuration and performance of the data
701 assimilation system, *Quarterly Journal of the royal meteorological society*, 137, 553-597,
702 <https://doi.org/10.1002/qj.828>, 2011.
- 703 Dey, S., Di Girolamo, L., Zhao, G., Jones, A. L., and McFarquhar, G. M.: Satellite-observed
704 relationships between aerosol and trade-wind cumulus cloud properties over the Indian Ocean,
705 *Geophysical Research Letters*, 38, <https://doi.org/10.1029/2010GL045588>, 2011.
- 706 Emanuel, K. A., Neelin, J. D., and Bretherton, C. S.: On large-scale circulations in convecting
707 atmospheres, *Quarterly Journal of the Royal Meteorological Society*, 120, 1111-1143, 1994.



- 708 Fan, J., Zhang, R., Li, G., and Tao, W.-K.: Effects of aerosols and relative humidity on cumulus clouds,
709 *Journal of Geophysical Research-Atmospheres*, 112, 10.1029/2006jd008136, 2007.
- 710 Fan, J., Yuan, T., Comstock, J. M., Ghan, S., Khain, A., Leung, L. R., Li, Z., Martins, V. J., and
711 Ovchinnikov, M.: Dominant role by vertical wind shear in regulating aerosol effects on deep
712 convective clouds, *Journal of Geophysical Research-Atmospheres*, 114, 10.1029/2009jd012352,
713 2009.
- 714 Fan, J., Comstock, J. M., and Ovchinnikov, M.: The cloud condensation nuclei and ice nuclei effects
715 on tropical anvil characteristics and water vapor of the tropical tropopause layer, *Environmental*
716 *Research Letters*, 5, 10.1088/1748-9326/5/4/044005, 2010.
- 717 Fan, J., Leung, L. R., Rosenfeld, D., Chen, Q., Li, Z., Zhang, J., and Yan, H.: Microphysical effects
718 determine macrophysical response for aerosol impacts on deep convective clouds, *Proceedings of*
719 *the National Academy of Sciences*, 110, E4581-E4590, <https://doi.org/10.1073/pnas.1316830110>,
720 2013.
- 721 Fan, J., Wang, Y., Rosenfeld, D., and Liu, X.: Review of aerosol–cloud interactions: Mechanisms,
722 significance, and challenges, *Journal of the Atmospheric Sciences*, 73, 4221-4252,
723 <https://doi.org/10.1175/JAS-D-16-0037.1>, 2016.
- 724 Ghan, S. J., Abdul-Razzak, H., Nenes, A., Ming, Y., Liu, X., Ovchinnikov, M., Shipway, B., Meskhidze,
725 N., Xu, J., and Shi, X.: Droplet nucleation: Physically-based parameterizations and comparative
726 evaluation, *Journal of Advances in Modeling Earth Systems*, 3,
727 <https://doi.org/10.1029/2011MS000074>, 2011.
- 728 Glassmeier, F., and Lohmann, U.: Constraining precipitation susceptibility of warm-, ice-, and mixed-
729 phase clouds with microphysical equations, *Journal of the Atmospheric Sciences*, 73, 5003-5023,
730 <https://doi.org/10.1175/JAS-D-16-0008.1>, 2016.
- 731 Goren, T., and Rosenfeld, D.: Decomposing aerosol cloud radiative effects into cloud cover, liquid
732 water path and Twomey components in marine stratocumulus, *Atmospheric research*, 138, 378-393,
733 <https://doi.org/10.1016/j.atmosres.2013.12.008>, 2014.
- 734 Grabowski, W. W., and Morrison, H.: Untangling microphysical impacts on deep convection applying
735 a novel modeling methodology. Part II: Double-moment microphysics, *Journal of the Atmospheric*
736 *Sciences*, 73, 3749-3770, <https://doi.org/10.1175/JAS-D-15-0367.1>, 2016.
- 737 Gryspeerdt, E., and Stier, P.: Regime-based analysis of aerosol-cloud interactions, *Geophysical*
738 *Research Letters*, 39, <https://doi.org/10.1029/2012GL053221>, 2012.
- 739 Gryspeerdt, E., Stier, P., White, B., and Kipling, Z.: Wet scavenging limits the detection of aerosol
740 effects on precipitation, *Atmospheric Chemistry and Physics*, 15, 7557-7570,
741 <https://doi.org/10.5194/acp-15-7557-2015>, 2015.
- 742 Gryspeerdt, E., Sourdeval, O., Quaas, J., Delanoë, J., Krämer, M., and Kühne, P.: Ice crystal number
743 concentration estimates from lidar–radar satellite remote sensing–Part 2: Controls on the ice crystal
744 number concentration, *Atmospheric Chemistry and Physics*, 18, 14351-14370,
745 <https://doi.org/10.5194/acp-18-14351-2018>, 2018b.
- 746 Gryspeerdt, E., Goren, T., Sourdeval, O., Quaas, J., Mülmenstädt, J., Dipu, S., Unglaub, C., Gettelman,
747 A., and Christensen, M.: Constraining the aerosol influence on cloud liquid water path, *Atmospheric*
748 *Chemistry and Physics*, 19, 5331-5347, <https://doi.org/10.5194/acp-19-5331-2019>, 2019.
- 749 Heikenfeld, M., White, B., Labbouz, L., and Stier, P.: Aerosol effects on deep convection: the
750 propagation of aerosol perturbations through convective cloud microphysics, *Atmospheric*
751 *Chemistry and Physics*, 19, 2601-2627, <https://doi.org/10.5194/acp-19-2601-2019>, 2019.



- 752 Henderson, D. S., L'Ecuyer, T., Stephens, G., Partain, P., and Sekiguchi, M.: A Multisensor Perspective
753 on the Radiative Im- pacts of Clouds and Aerosols, *J. Appl. Meteorol. Clim.*, 52, 853– 871,
754 <https://doi.org/10.1175/JAMC-D-12-025.1>, 2013.
- 755 Hodnebrog, O., Myhre, G., Forster, P. M., Sillmann, J., and Samset, B. H.: Local biomass burning is a
756 dominant cause of the observed precipitation reduction in southern Africa, *Nat Commun*, 7,
757 10.1038/ncomms11236, 2016.
- 758 Hoose, C., and Möhler, O.: Heterogeneous ice nucleation on atmospheric aerosols: a review of
759 results from laboratory experiments, *Atmo-30 spheric Chemistry and Physics*, 12, 9817–9854. 2012.
- 760 Iacono, M. J., Delamere, J. S., Mlawer, E. J., Shephard, M. W., Clough, S. A., and Collins, W. D.:
761 Radiative forcing by long-lived greenhouse gases: Calculations with the AER radiative transfer
762 models, *Journal of Geophysical Research: Atmospheres*, 113,
763 <https://doi.org/10.1029/2008JD009944>, 2008.
- 764 Jakob, C., Singh, M., and Jungandreas, L.: Radiative Convective Equilibrium and Organized
765 Convection: An Observational Perspective, *Journal of Geophysical Research: Atmospheres*, 124,
766 5418-5430, 2019.
- 767 Jeon, Y.-L., Moon, S., Lee, H., Baik, J.-J., and Lkhamjav, J.: Non-Monotonic Dependencies of Cloud
768 Microphysics and Precipitation on Aerosol Loading in Deep Convective Clouds: A Case Study Using
769 the WRF Model with Bin Microphysics, *Atmosphere*, 9, 434, <https://doi.org/10.3390/atmos9110434>,
770 2018.
- 771 Jiang, H., Xue, H., Teller, A., Feingold, G., and Levin, Z.: Aerosol effects on the lifetime of shallow
772 cumulus, *Geophysical Research Letters*, 33, 10.1029/2006gl026024, 2006.
- 773 Jiang, J. H., Su, H., Huang, L., Wang, Y., Massie, S., Zhao, B., Omar, A., and Wang, Z.: Contrasting
774 effects on deep convective clouds by different types of aerosols, *Nature communications*, 9, 3874,
775 2018.
- 776 Kalina, E. A., Friedrich, K., Morrison, H., and Bryan, G. H.: Aerosol effects on idealized supercell
777 thunderstorms in different environments, *Journal of the Atmospheric Sciences*, 71, 4558-4580,
778 <https://doi.org/10.1175/JAS-D-14-0037.1>, 2014.
- 779 Kaufman, Y. J., Koren, I., Remer, L. A., Rosenfeld, D., and Rudich, Y.: The effect of smoke, dust, and
780 pollution aerosol on shallow cloud development over the Atlantic Ocean, *Proceedings of the*
781 *National Academy of Sciences of the United States of America*, 102, 11207-11212,
782 10.1073/pnas.0505191102, 2005.
- 783 Khain, A., Rosenfeld, D., and Pokrovsky, A.: Aerosol impact on the dynamics and microphysics of
784 deep convective clouds, *Quarterly Journal of the Royal Meteorological Society*, 131, 2639-2663,
785 10.1256/qj.04.62, 2005.
- 786 Khain, A., Beheng, K., Heymsfield, A., Korolev, A., Krichak, S., Levin, Z., Pinsky, M., Phillips, V.,
787 Prabhakaran, T., and Teller, A.: Representation of microphysical processes in cloud-resolving models:
788 spectral (bin) microphysics vs. bulk parameterization, *Reviews of Geophysics*,
789 <https://doi.org/10.1002/2014RG000468>, 2015.
- 790 Khain, A. P., BenMoshe, N., and Pokrovsky, A.: Factors determining the impact of aerosols on surface
791 precipitation from clouds: An attempt at classification, *Journal of the Atmospheric Sciences*, 65,
792 1721-1748, 10.1175/2007jas2515.1, 2008.
- 793 Khain, A. P.: Notes on state-of-the-art investigations of aerosol effects on precipitation: a critical
794 review, *Environmental Research Letters*, 4, 015004 (015020 pp.)-015004 (015020 pp.),
795 10.1088/1748-9326/4/1/015004, 2009.



- 796 Kipling, Z., Stier, P., Labbouz, L., and Wagner, T.: Dynamic subgrid heterogeneity of convective cloud
797 in a global model: description and evaluation of the Convective Cloud Field Model (CCFM) in
798 ECHAM6–HAM2, *Atmospheric Chemistry and Physics*, 17, 327–342, [https://doi.org/10.5194/acp-17-](https://doi.org/10.5194/acp-17-327-2017)
799 [327-2017](https://doi.org/10.5194/acp-17-327-2017), 2017.
- 800 Klepp, C., Ament, F., Bakan, S., Hirsch, L., and Stevens, B.: The NARVAL Campaign Report, 2014.
- 801 Klocke, D., Brueck, M., Hohenegger, C., and Stevens, B.: Rediscovery of the doldrums in storm-
802 resolving simulations over the tropical Atlantic, *Nature Geoscience*, 10, 891, 2017.
- 803 Koren, I., Kaufman, Y. J., Rosenfeld, D., Remer, L. A., and Rudich, Y.: Aerosol invigoration and
804 restructuring of Atlantic convective clouds, *Geophysical Research Letters*, 32,
805 10.1029/2005gl023187, 2005.
- 806 Koren, I., Remer, L. A., Altaratz, O., Martins, J. V., and Davidi, A.: Aerosol-induced changes of
807 convective cloud anvils produce strong climate warming, *Atmospheric Chemistry and Physics*, 10,
808 5001–5010, 10.5194/acp-10-5001-2010, 2010.
- 809 Koren, I., Dagan, G., and Altaratz, O.: From aerosol-limited to invigoration of warm convective
810 clouds, *science*, 344, 1143–1146, DOI: 10.1126/science.1252595, 2014.
- 811 Koren, I., Altaratz, O., and Dagan, G.: Aerosol effect on the mobility of cloud droplets, *Environmental*
812 *Research Letters*, 10, 104011, doi:10.1088/1748-9326/10/10/104011, 2015.
- 813 Labbouz, L., Kipling, Z., Stier, P., and Protat, A.: How Well Can We Represent the Spectrum of
814 Convective Clouds in a Climate Model? Comparisons between Internal Parameterization Variables
815 and Radar Observations, *Journal of the Atmospheric Sciences*, 75, 1509–1524,
816 <https://doi.org/10.1175/JAS-D-17-0191.1>, 2018.
- 817 Lebo, Z. J., and Morrison, H.: Dynamical effects of aerosol perturbations on simulated idealized
818 squall lines, *Monthly Weather Review*, 142, 991–1009, 2014.
- 819 Lee, S.-S., Feingold, G., and Chuang, P. Y.: Effect of aerosol on cloud–environment interactions in
820 trade cumulus, *Journal of the Atmospheric Sciences*, 69, 3607–3632, 2012.
- 821 Lee, S. S., Donner, L. J., and Phillips, V. T. J.: Sensitivity of aerosol and cloud effects on radiation to
822 cloud types: comparison between deep convective clouds and warm stratiform clouds over one-day
823 period, *Atmospheric Chemistry and Physics*, 9, 2555–2575, 2009.
- 824 Levin, Z., and Cotton, W. R.: *Aerosol pollution impact on precipitation: A scientific review*, Springer,
825 2009.
- 826 Liu, H., Guo, J., Koren, I., Altaratz, O., Dagan, G., Wang, Y., Jiang, J. H., Zhai, P., and Yung, Y. L.: Non-
827 Monotonic Aerosol Effect on Precipitation in Convective Clouds over Tropical Oceans, *Scientific*
828 *Reports*, 9, 7809, 2019.
- 829 Liu, L., Shawki, D., Voulgarakis, A., Kasoar, M., Samset, B., Myhre, G., Forster, P., Hodnebrog, Ø.,
830 Sillmann, J., and Aalbergstjø, S.: A PDRMIP Multimodel Study on the impacts of regional aerosol
831 forcings on global and regional precipitation, *Journal of Climate*, 31, 4429–4447, 2018.
- 832 Lohmann, U., and Hoose, C.: Sensitivity studies of different aerosol indirect effects in mixed-phase
833 clouds, *Atmospheric Chemistry and Physics*, 9, 8917–8934, 2009.
- 834 Manabe, S., and Strickler, R. F.: Thermal equilibrium of the atmosphere with a convective
835 adjustment, *Journal of the Atmospheric Sciences*, 21, 361–385, 1964
- 836 Mlawer, E. J., Taubman, S. J., Brown, P. D., Iacono, M. J., and Clough, S. A.: Radiative transfer for
837 inhomogeneous atmospheres: RRTM, a validated correlated-k model for the longwave, *Journal of*
838 *Geophysical Research: Atmospheres*, 102, 16663–16682, 1997.
- 839 Muller, C., and O’Gorman, P.: An energetic perspective on the regional response of precipitation to
840 climate change, *Nature Climate Change*, 1, 266, 2011.



- 841 Mülmenstädt, J., and Feingold, G.: The Radiative Forcing of Aerosol–Cloud Interactions in Liquid
842 Clouds: Wrestling and Embracing Uncertainty, *Current Climate Change Reports*, 4, 23–40,
843 <https://doi.org/10.1007/s40641-018-0089-y>, 2018.
- 844 Myhre, G., Forster, P., Samset, B., Hodnebrog, Ø., Sillmann, J., Aalbergsjø, S., Andrews, T., Boucher,
845 O., Faluvegi, G., and Fläschner, D.: PDRMIP: a precipitation driver and response model
846 intercomparison project—protocol and preliminary results, *Bulletin of the American Meteorological*
847 *Society*, 98, 1185–1198, 2017.
- 848 O’Gorman, P. A., Allan, R. P., Byrne, M. P., and Previdi, M.: Energetic Constraints on Precipitation
849 Under Climate Change, *Surveys in Geophysics*, 33, 585–608, <https://doi.org/10.1007/s10712-011-850-9159-6>, 2012.
- 851 Ovchinnikov, M., Ackerman, A. S., Avramov, A., Cheng, A., Fan, J., Fridlind, A. M., Ghan, S.,
852 Harrington, J., Hoose, C., and Korolev, A.: Intercomparison of large-eddy simulations of Arctic mixed-
853 phase clouds: Importance of ice size distribution assumptions, *Journal of Advances in Modeling Earth*
854 *Systems*, 6, 223–248, <https://doi.org/10.1002/2013MS000282>, 2014.
- 855 Richardson, T., Forster, P., Andrews, T., Boucher, O., Faluvegi, G., Fläschner, D., Hodnebrog, Ø.,
856 Kasoar, M., Kirkevåg, A., and Lamarque, J.-F.: Drivers of precipitation change: An energetic
857 understanding, *Journal of Climate*, 31, 9641–9657, <https://doi.org/10.1175/JCLI-D-17-0240.1>, 2018.
- 858 Rosenfeld, D.: Suppression of rain and snow by urban and industrial air pollution, *Science*, 287, 1793–
859 1796, [10.1126/science.287.5459.1793](https://doi.org/10.1126/science.287.5459.1793), 2000.
- 860 Rosenfeld, D., Lohmann, U., Raga, G. B., O’Dowd, C. D., Kulmala, M., Fuzzi, S., Reissell, A., and
861 Andreae, M. O.: Flood or drought: How do aerosols affect precipitation?, *Science*, 321, 1309–1313,
862 [10.1126/science.1160606](https://doi.org/10.1126/science.1160606), 2008.
- 863 Rosenfeld, D., Wood, R., Donner, L. J., and Sherwood, S. C.: Aerosol cloud-mediated radiative forcing:
864 highly uncertain and opposite effects from shallow and deep clouds, in: *Climate Science for Serving*
865 *Society*, Springer, 105–149, https://doi.org/10.1007/978-94-007-6692-1_5, 2013.
- 866 Rosenfeld, D., Zhu, Y., Wang, M., Zheng, Y., Goren, T., and Yu, S.: Aerosol-driven droplet
867 concentrations dominate coverage and water of oceanic low-level clouds, *Science*, 363, eaav0566,
868 DOI: [10.1126/science.aav0566](https://doi.org/10.1126/science.aav0566), 2019.
- 869 Rothenberg, D., Avramov, A., and Wang, C.: On the representation of aerosol activation and its
870 influence on model-derived estimates of the aerosol indirect effect, *Atmos. Chem. Phys*, 18, 7961–
871 7983, <https://doi.org/10.5194/acp-18-7961-2018>, 2018.
- 872 Samset, B., Myhre, G., Forster, P., Hodnebrog, Ø., Andrews, T., Faluvegi, G., Flaeschner, D., Kasoar,
873 M., Kharin, V., and Kirkevåg, A.: Fast and slow precipitation responses to individual climate forcings: A
874 PDRMIP multimodel study, *Geophysical Research Letters*, 43, 2782–2791,
875 <https://doi.org/10.1002/2016GL068064>, 2016.
- 876 Savane, O. S., Vant-Hull, B., Mahani, S., and Khanbilvardi, R.: Effects of Aerosol on Cloud Liquid
877 Water Path: Statistical Method a Potential Source for Divergence in Past Observation Based
878 Correlative Studies, *Atmosphere*, 6, 273–298, <https://doi.org/10.3390/atmos6030273>, 2015.
- 879 Seifert, A., and Beheng, K.: A two-moment cloud microphysics parameterization for mixed-phase
880 clouds. Part 2: Maritime vs. continental deep convective storms, *Meteorology and Atmospheric*
881 *Physics*, 92, 67–82, <https://doi.org/10.1007/s00703-005-0113-3>, 2006a.
- 882 Seifert, A., and Beheng, K. D.: A two-moment cloud microphysics parameterization for mixed-phase
883 clouds. Part 1: Model description, *Meteorology and atmospheric physics*, 92, 45–66,
884 <https://doi.org/10.1007/s00703-005-0112-4>, 2006b.



- 885 Seifert, A., and Heus, T.: Large-eddy simulation of organized precipitating trade wind cumulus
886 clouds, *Atmos. Chem. Phys.*, 13, 5631-5645, doi:10.5194/acpd-13-1855-2013, 2013.
- 887 Seifert, A., Heus, T., Pincus, R., and Stevens, B.: Large-eddy simulation of the transient and near-
888 equilibrium behavior of precipitating shallow convection, *Journal of Advances in Modeling Earth*
889 *Systems*, <https://doi.org/10.1002/2015MS000489>, 2015.
- 890 Seigel, R. B.: Shallow Cumulus Mixing and Subcloud Layer Responses to Variations in Aerosol
891 Loading, *Journal of the Atmospheric Sciences*, <https://doi.org/10.1175/JAS-D-13-0352.1>, 2014.
- 892 Simpson, E., Connolly, P., and McFiggans, G.: An investigation into the performance of four cloud
893 droplet activation parameterisations, *Geoscientific Model Development*, 7, 1535-1542,
894 doi:10.5194/gmd-7-1535-2014, 2014.
- 895 Small, J. D., Chuang, P. Y., Feingold, G., and Jiang, H.: Can aerosol decrease cloud lifetime?,
896 *Geophysical Research Letters*, 36, <https://doi.org/10.1029/2009GL038888>, 2009.
- 897 Sourdeval, O., Gryspeerdt, E., Krämer, M., Goren, T., Delanoë, J., Afchine, A., Hemmer, F., and Quaas,
898 J.: Ice crystal number concentration estimates from lidar–radar satellite remote sensing—Part 1:
899 Method and evaluation, <https://doi.org/10.5194/acp-18-14327-2018> 2018.
- 900 Spill, G., Stier, P., Field, P. R., and Dagan, G.: Effects of aerosol in simulations of realistic shallow
901 cumulus cloud fields in a large domain, *Atmospheric Chemistry and Physics*,
902 <https://doi.org/10.5194/acp-2019-432>, 2019.
- 903 Stephens, G. L., Gabriel, P. M., and Partain, P. T.: Parameterization of atmospheric radiative transfer.
904 Part I: Validity of simple models, *Journal of the atmospheric sciences*, 58, 3391-3409,
905 [https://doi.org/10.1175/1520-0469\(2001\)058%3C3391:POARTP%3E2.0.CO;2](https://doi.org/10.1175/1520-0469(2001)058%3C3391:POARTP%3E2.0.CO;2), 2001.
- 906 Stevens, B., and Feingold, G.: Untangling aerosol effects on clouds and precipitation in a buffered
907 system, *Nature*, 461, 607-613, 10.1038/nature08281, 2009.
- 908 Stevens, B., Farrell, D., Hirsch, L., Jansen, F., Nuijens, L., Serikov, I., Brüggemann, B., Forde, M., Linne,
909 H., and Lonitz, K.: The Barbados Cloud Observatory: Anchoring investigations of clouds and
910 circulation on the edge of the ITCZ, *Bulletin of the American Meteorological Society*, 97, 787-801,
911 2016.
- 912 Stevens, B., Ament, F., Bony, S., Crewell, S., Ewald, F., Gross, S., Hansen, A., Hirsch, L., Jacob, M., and
913 Kölling, T.: A high-altitude long-range aircraft configured as a cloud observatory—the NARVAL
914 expeditions, *Bulletin of the American Meteorological Society*, <https://doi.org/10.1175/BAMS-D-18-0198.1>, 2019.
- 916 Storelvmo, T., Hoose, C., and Eriksson, P.: Global modeling of mixed-phase clouds: The albedo and
917 lifetime effects of aerosols, *Journal of Geophysical Research: Atmospheres*, 116,
918 <https://doi.org/10.1029/2010JD014724>, 2011.
- 919 Tao, W.-K., Chen, J.-P., Li, Z., Wang, C., and Zhang, C.: Impact of aerosols on convective clouds and
920 precipitation, *Reviews of Geophysics*, 50, RG2001, <https://doi.org/10.1029/2011RG000369>, 2012.
- 921 Twomey, S.: The influence of pollution on the shortwave albedo of clouds, *Journal of the*
922 *atmospheric sciences*, 34, 1149-1152, 1977.
- 923 van den Heever, S. C., Stephens, G. L., and Wood, N. B.: Aerosol Indirect Effects on Tropical
924 Convection Characteristics under Conditions of Radiative–Convective Equilibrium, *Journal of the*
925 *Atmospheric Sciences*, 68, 699-718, 10.1175/2010jas3603.1, 2011.
- 926 Varble, A.: Erroneous attribution of deep convective invigoration to aerosol concentration, *Journal*
927 *of the Atmospheric Sciences*, 75, 1351-1368, <https://doi.org/10.1175/JAS-D-17-0217.1>, 2018.



928 White, B., Gryspeerdt, E., Stier, P., Morrison, H., Thompson, G., and Kipling, Z.: Uncertainty from
929 choice of microphysics scheme in convection-permitting models significantly exceeds aerosol effects,
930 Atmospheric Chemistry and Physics, 7, <https://doi.org/10.5194/acp-17-12145-2017>, 2017.
931 Williams, E., Rosenfeld, D., Madden, N., Gerlach, J., Gears, N., Atkinson, L., Dunnemann, N.,
932 Frostrom, G., Antonio, M., and Biazon, B.: Contrasting convective regimes over the Amazon:
933 Implications for cloud electrification, J. Geophys. Res, 107, <https://doi.org/10.1029/2001JD000380>,
934 2002.
935 Xue, H., and Feingold, G.: Large-eddy simulations of trade wind cumuli: Investigation of aerosol
936 indirect effects, Journal of the atmospheric sciences, 63, 1605-1622,
937 <https://doi.org/10.1175/JAS3706.1>, 2006.
938 Yuan, T., Remer, L. A., Pickering, K. E., and Yu, H.: Observational evidence of aerosol enhancement of
939 lightning activity and convective invigoration, Geophysical Research Letters, 38,
940 10.1029/2010gl046052, 2011a.
941 Yuan, T., Remer, L. A., and Yu, H.: Microphysical, macrophysical and radiative signatures of volcanic
942 aerosols in trade wind cumulus observed by the A-Train, Atmospheric Chemistry and Physics, 11,
943 7119-7132, 10.5194/acp-11-7119-2011, 2011b.
944 Zängl, G., Reinert, D., Rípodas, P., and Baldauf, M.: The ICON (ICOsahedral Non-hydrostatic)
945 modelling framework of DWD and MPI-M: Description of the non-hydrostatic dynamical core,
946 Quarterly Journal of the Royal Meteorological Society, 141, 563-579,
947 <https://doi.org/10.1002/qj.2378>, 2015.
948